



Turbulent Radiation Effects in HSCT Combustor Rich Zone

Robert J. Hall

United Technologies Research Corporation, Pratt & Whitney, East Hartford, Connecticut

Alexander Vranos and Weiduo Yu

University of Connecticut, Storrs, Connecticut

Prepared under Contract NAS3-26618

National Aeronautics and
Space Administration

Lewis Research Center

Available from

NASA Center for Aerospace Information
800 Elkridge Landing Road
Linthicum Heights, MD 21090-2934
Price Code: A05

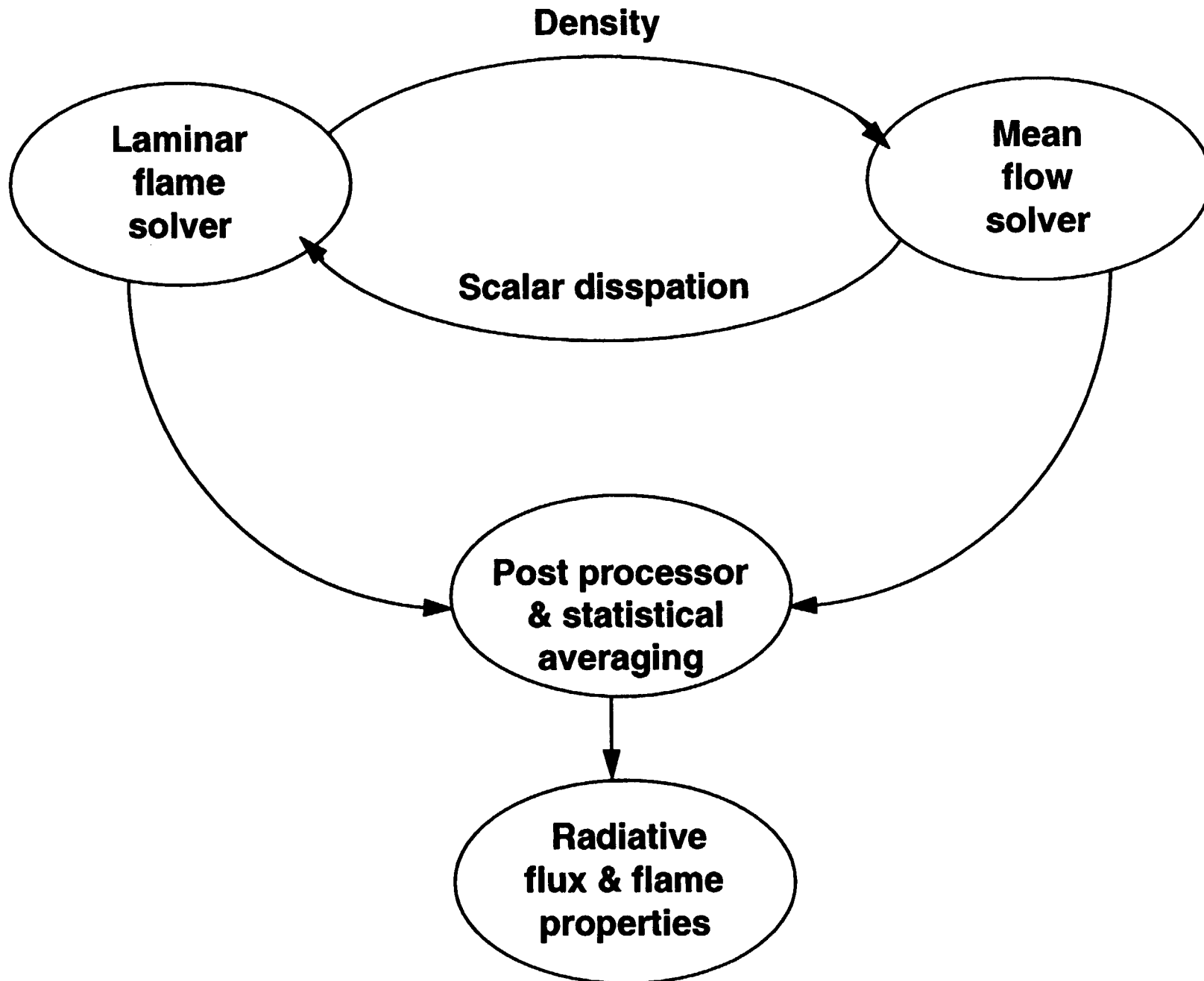
National Technical Information Service
5287 Port Royal Road
Springfield, VA 22100
Price Code: A05

INTRODUCTION

The RBQQ rich zone will be characterized by conditions that exacerbate thermal radiation loads on the liners. High soot densities and temperatures in the rich zone may lead to unacceptably high radiative fluxes which compromise liner durability. The task of predicting these radiative fluxes is complicated not just by the lack of good models for soot formation in jet fuel, but also by flow turbulence, which is known to lead to enhancement of radiation. Basing radiative calculations on time-averaged CFD temperatures and species densities will generally not be accurate. The development of a useful analytical tool for thermal heat transfer prediction thus requires a jet fuel kinetics scheme, a soot formation model, and an efficient way of calculating radiative fluxes in turbulent environments. The soot model is needed not just for prediction of radiation loads, but also for prediction of soot burnout in the quench zone. A further requirement is geometric flexibility for the radiation algorithm.

In response to this problem, a joint UTRC-University of Connecticut theoretical program was put in place. The program was based on describing coupled soot formation and radiation in turbulent flows using stretched flamelet theory. The University of Connecticut had responsibility for Subtask F, entitled Reactive Flow Modelling, and consisting of three parts: development of an engineering model of jet fuel kinetics appropriate to diffusive combustion, improvement of the standard, linear $k-\epsilon$ turbulence model which is common to many flow and combustion codes, and development of a joint pdf methodology for the calculation of mean flow and radiation in a turbulent flame. UTRC had responsibility for Subtask G, entitled Flamelet Kinetics and Turbulent Radiation Model. This effort was involved with using the model jet fuel kinetics mechanism to predict soot growth in flamelets at elevated pressure, to incorporate an efficient model for turbulent thermal radiation into a discrete transfer radiation code, and to couple the soot growth, flowfield, and radiation algorithms. The soot calculations used a recently developed opposed jet code which couples the dynamical equations of size-class dependent particle growth with complex chemistry.

Several of the tasks represent technical firsts; among these are the prediction of soot from a detailed jet fuel kinetics mechanism, the inclusion of pressure effects in the soot particle growth equations, and the inclusion of the efficient turbulent radiation algorithm in a combustor code. A schematic overview of the main technical tasks and how they are coupled to provide predictions of radiative fluxes is shown in the accompanying figure, followed by detailed descriptions of the work done in the two Subtasks, the soot growth/radiation computer program, and sample calculations.



Subtask F. Reactive Flow Modeling

The reactive flow modeling task consisted of three parts: development of a jet fuel kinetics model appropriate to diffusive combustion, improvement of the standard, linear k-e turbulence model which is common to many flow and combustion codes, and development of a joint pdf methodology for the calculation of mean flow and radiation in a turbulent flame. The underlying combustion model is based on flamelet theory and is described below.

FLAMELET MODELING

Turbulent combustion modeling necessitates dealing with the description of reaction rates, directly or indirectly. Advanced combustion models seek to circumvent the problem of solving balance equations and associated closure problems involving scalar correlations which appear in a conventional Reynolds decomposition of the species conservation equations.

Of the more advanced methods flamelet and PDF methods are the most promising. PDF methods potentially have greater generality, but are mathematically more complex than flamelet models and presently are limited to very simple chemistry. The latter limitation precludes the modeling of soot formation from large hydrocarbon molecules. Modeling of turbulence/radiation effects using PDF methods also is expected to be especially cumbersome. On the other hand, flamelet modeling, the approach followed in this work, easily accommodates complex chemistry and radiation effects. Although in certain applications the principal constraint in flamelet modeling may be a physical one, that the scale of the reaction zone need be small relative to the scale of turbulence, this is not expected to be a limitation in modeling high pressure, high temperature flames as found in gas turbine combustors.

In flamelet modeling, the combustion zone is treated as an ensemble of folded, laminar-like structures which are convected by the turbulence. The thickness of the laminar-like reaction zone is a function of the strain rate as reflected in the molecular (scalar) dissipation, a quantity analogous to the viscous dissipation. Both the mean scalar and viscous dissipation are computed in the mean

flow calculation.

A highly significant advantage of the flamelet approach is that kinetic calculations are not carried out in the main flow calculation. Thus unencumbered, the problem is reduced to computation of mixing with variable density. Luminous and non-luminous radiation, intensity combustion products, and soot concentrations are derived from post-processing of the main flow data using analytical expressions for these properties derived from a laminar flamelet calculation.

JET FUEL KINETICS

The objective of this task was to develop a kinetics scheme which provides realistic estimates of flamelet temperature and flame products concentrations necessary for the prediction of both luminous and non-luminous radiation. The prediction of intermediates, particularly acetylene and aromatics, was considered essential for the description of soot formation. To keep this task manageable under the allotted time it was necessary to do two things. The first was to decide upon the composition of the simplest model fuel which might mimic the behavior of jet fuel, and the second was to devise a kinetics scheme for the model fuel. Both pyrolysis and oxidation kinetics were considered. Regarding the latter, simple, global kinetic schemes, as described in the literature, were not considered adequate for two reasons, the lack of description of intermediates necessary to describe the formation of soot, and the limited range of pressure, temperature and composition over which global schemes are valid. Furthermore, diffusive effects, not reflected in global schemes, are important in practical devices. The development of "jet fuel kinetics" therefore necessitated considering both complex pyrolysis and oxidation kinetics keeping in mind that combustion would occur primarily in a diffusive (as opposed to premixed) mode. This latter assumption allowed a major simplification of the kinetics scheme. The kinetics scheme and its inclusion in the flamelet calculation is discussed below.

MODEL FUEL SELECTION

One important consideration in devising a model fuel is that the fuel should mimic the combustion of jet fuel in the formation of soot. The appropriate physical model of soot formation is that soot derives from the inception and subsequent growth of soot nuclei originating in fuel-rich zones. The inception process consists of the formation of polycyclic aromatics (PAH) under fuel-rich conditions followed by the growth of PAH from the continuous addition of acetylene to the PAH. Eventually a solid phase is formed which also grows grow by acetylene addition. Soot kinetics are discussed in Subtask G, where a detailed description of the soot formation model used in this work is given.

Since jet fuel contains about 20% aromatics, incepting species are abundant initially, and the inclusion of an aromatics component in the model fuel is essential. Acetylene is a product of the pyrolysis of the alkane constituents, the most abundant family of compounds in jet fuel. Although the alkane fraction consists of hundreds of compounds, individual alkanes will pyrolyze in a similar manner to yield ethylene, methane, hydrogen, and most significantly, acetylene. Thus, a simple model fuel would consist of two classes of compounds, alkanes and aromatics, and the simplest model fuel would contain a single representative alkane and a single representative aromatic.

Detailed chemical analyses provided by Southern Petroleum Laboratories and Pratt and Whitney Aircraft were the principal sources considered in devising the model fuel. Total saturates and aromatics and the most abundant carbon number for each class are shown in Table 1.

Table 1

	<u>P&W</u>	<u>SPL</u>	<u>Average Carbon Number</u>	<u>Most Abundant</u>
Saturates	79.1	76.6	9.98	C ₁₀
Aromatics	20.5	19.1	9.12	C ₉ , C ₁₀

N-decane and trimethylbenzene were selected as the model fuel components on the basis of average carbon number and the detailed analysis (85% n-decane, 15% trimethylbenzene). Contri-

butions to soot from other relatively abundant compounds, such as indans, tetralin, and naphthalenes were not considered as these could be considered as additive incepting species (see soot model). Cycloalkanes were not considered separately.

The overall kinetic scheme is summarized in Fig. 1. The reaction equation set is presented in Appendix A. This scheme was incorporated into the laminar flamelet calculation which provided flamelet temperature and gaseous species distributions. In a second step these data were used as the starting point for the calculation of soot via the UTRC soot model.

For n-decane, it was assumed that appreciable heating of the fuel in a diffusion flame occurs prior to exposure to oxygen. Thus a reasonable simplification would allow that substantial decane pyrolysis occurs before significant oxidation. The process was viewed as one in which decane served as a source of pyrolysis products, most of which were subsequently oxidized and a small fraction of which (C_2H_2) participated in the formation of soot. Oxidation was confined to C1 and C2 species. The n-decane kinetics are modeled through a step-wise pyrolysis scheme beginning with the formation of decyl radical and proceeding to the formation of smaller saturated and unsaturated molecules whose oxidation is modeled comprehensively. An abbreviated benzene formation/pyrolysis/oxidation scheme was used. The approach is opposite to that taken in describing decane kinetics. It was assumed that aromatic nuclei were thermally stable. Aromatics kinetics was modeled using a global oxidation scheme for 1,2,4 trimethyl benzene (TMB), the most abundant jet fuel aromatic constituent (Ref. 1). The mechanism describes the stepwise oxidation of mono-aromatic intermediates and decomposition to benzene (see Appendix A).

LAMINAR COUNTERFLOW FLAME (FLAMELET) CALCULATIONS

The kinetics scheme is incorporated into a laminar, counterflow, diffusion flame calculation which serves as the basis of the turbulent combustion model. The flamelet calculation is done for a counterflow diffusion flame with appropriate temperature, pressure, and mass flux boundary conditions for the fuel and oxidant streams. Mixture fraction is computed from the species profiles,

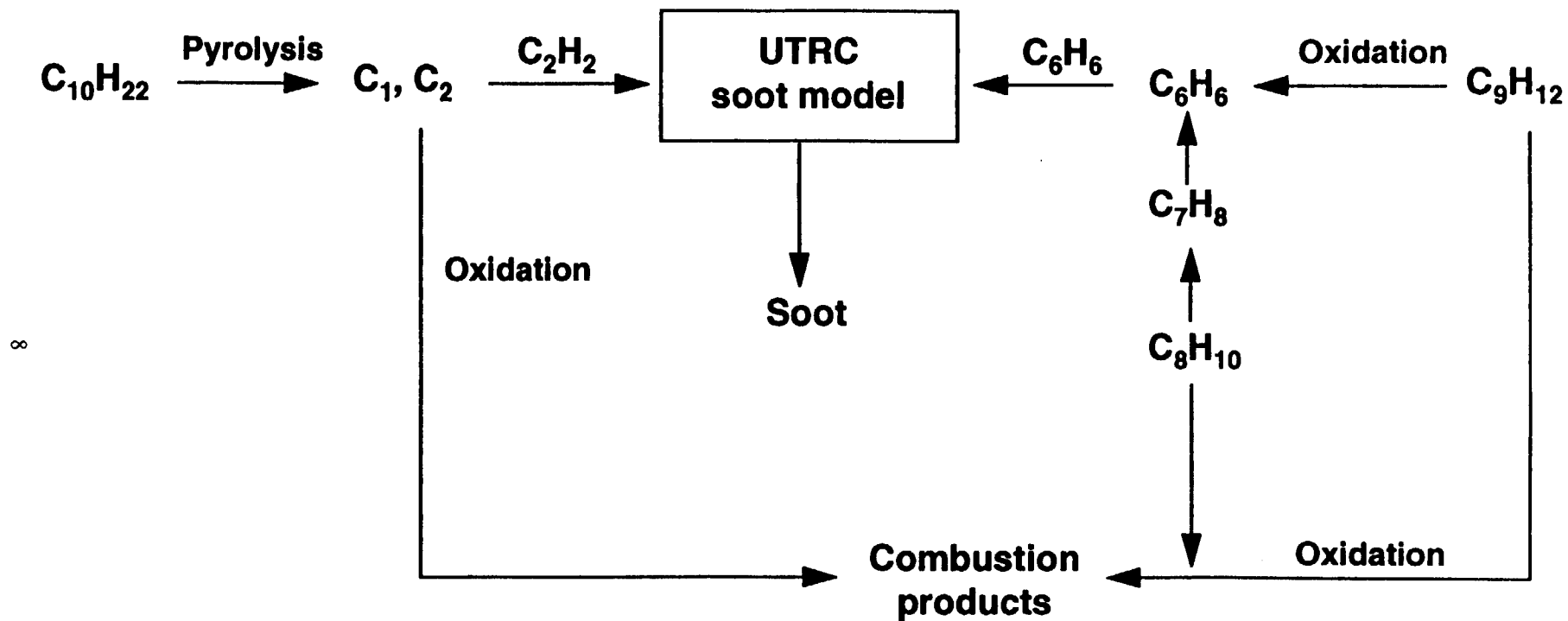


Figure 1. Model jet fuel kinetics schematic.

and the relevant species, temperature and density functions are expressed as polynomials in mixture fraction. Individual flamelet calculations are parameterized by the scalar dissipation rate which is a function of the reactant mass fluxes. Successful laminar flame solutions have been obtained with the model fuel. Substantial concentrations of benzene and acetylene are indicated. Typical flamelet profiles are shown in Fig. 2. Inspection of the data computed at typical engine operating conditions, indicate that the the heat release zone is very thin, about 0.3mm, thus supporting the flamelet model.

NON-LINEAR $k-\epsilon$ TURBULENCE MODEL

A non-linear $k-\epsilon$ turbulence model, based upon the work of Speziale (Refs. 2, 3), was incorporated into the TEACH code. The non-linear model provides a significant improvement in predictive capability over the standard $k-\epsilon$ model without significant additional computational burden. No additional equations are introduced into the analysis as with other advanced models such as differential Reynolds stress (DSM) algebraic stress (ASM) models. Notable successes of the model include improved prediction of normal stresses in channel flows, prediction of secondary flows in non-circular ducts (inherently impossible with the standard linear model), and improved prediction of recirculation zone length behind a rearward facing step.

The standard, linear $k-\epsilon$ model, assumes a linear relationship between stress and mean vorticity rendering it inherently unable to describe secondary and other flows with anisotropic normal stresses. For curved or swirling flows, correction terms are invoked in the dissipation equation and eddy viscosity formulation. Often these solutions are found to be problem dependent ,and thus, limited in generality. More advanced, (and also more complicated) approaches such as ASM and DSM may offer greater potential for complex flows, but this has not been established, and the additional computational burden often may not be justified. The non-linear stress model extends the validity of linear stress models by allowing for normal stress anisotropy. Two additional quadratic terms are added to the momentum stress expression. The additional terms are subject to several mathematical constraints, the principal restraint being that of frame indifference (Refs. 2, 3). This requires that

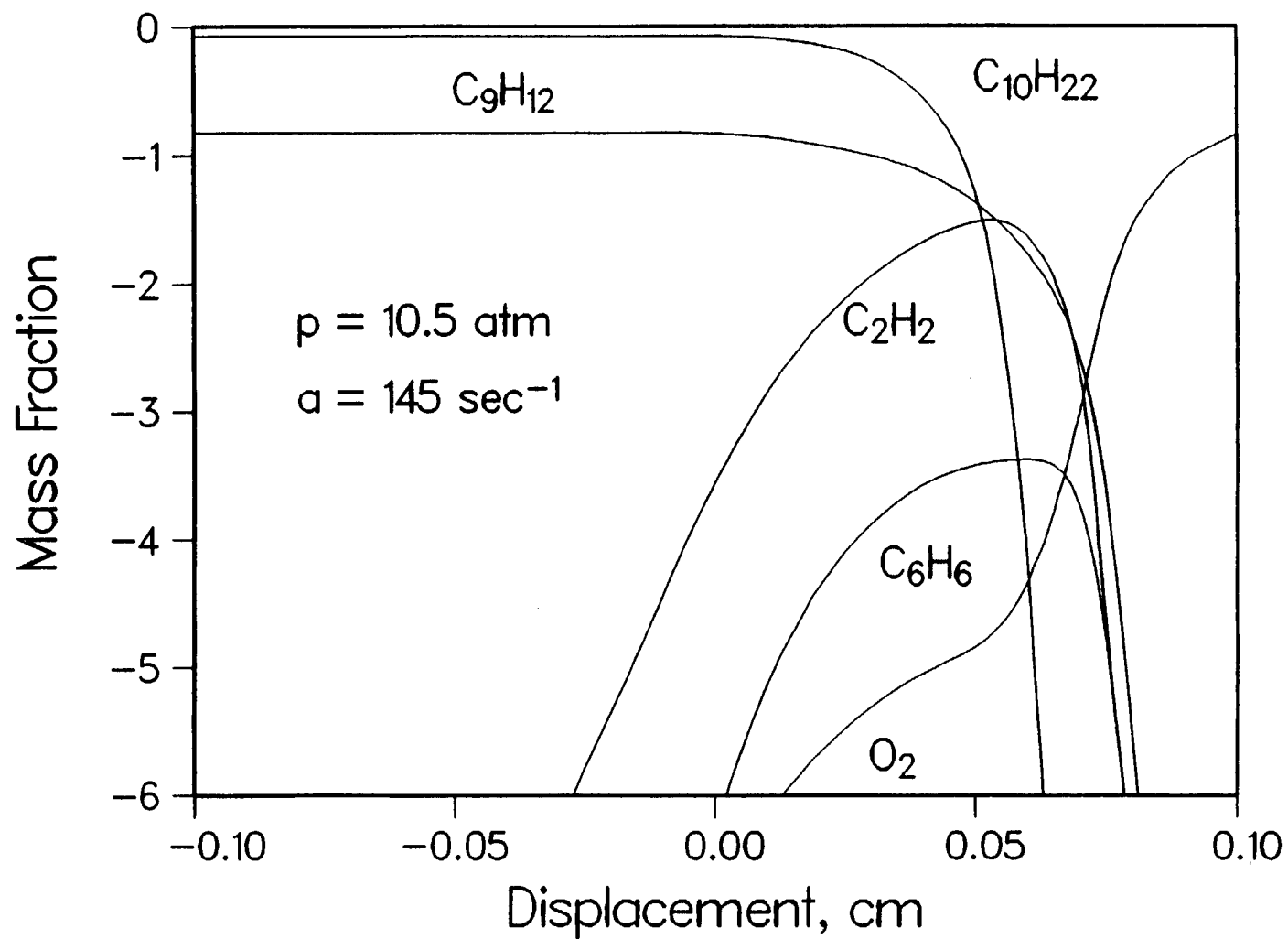


**Figure 2. Species profiles in model jet fuel flamelet.
Fuel: 15% trimethylbenzene, 85% decane**

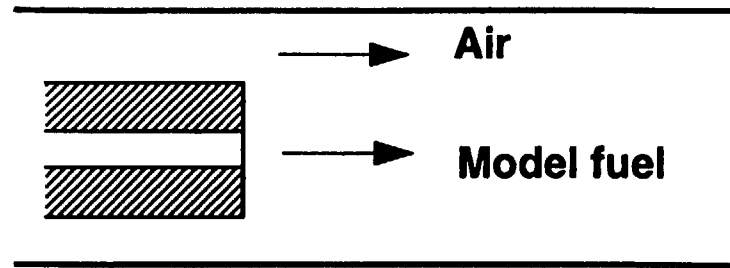
the tensor form of the non-linear terms not change with change of reference frame, i.e. the form is the same for both inertial and non-inertial reference frames. The expression is written below.

$$\begin{aligned}
\tau_{ij} = & -\frac{2}{3}\rho k\delta_{ij} + 2C\mu\rho\frac{\kappa^2}{\epsilon}\overline{D_{ij}} \\
& + C_D\rho(2C\mu)^2\frac{\kappa^3}{\epsilon^2}\left[\overline{D_{im}}\overline{D_{mj}} - 1/3\overline{D_{mn}}\overline{D_{mn}}\delta_{ij}\right. \\
& \left. + \overline{v} \cdot \nabla\overline{D_{ij}} - \frac{\partial v_i}{\partial \chi_{pz}}\overline{D_{kj}} - \frac{\partial v_j}{\partial \chi_k}\overline{D_{ki}}\right] \\
& + \frac{\delta_{ij}}{3}\left[\overline{v} \cdot \nabla\overline{D_{mk}} - 2\frac{\partial v_m}{\partial \chi^k}\overline{D_{mk}}\right]
\end{aligned} \tag{1}$$

where $\overline{D_{ij}}$ is the mean deformation tensor.

The constant C_D is assumed to have the value 1.68. The first two terms on the RHS represent the usual, linear formulation for the momentum stress; the remaining terms comprise the non-linear contribution. The expression above was rewritten for generalized coordinates and applied to a two-dimensional cylindrical system for application to the TEACH code. The principal difficulty in implementation is that a large number of quadratic terms are introduced when non-Cartesian coordinates are used.

Predictions of the linear and non-linear models are compared for a model fuel combustion in an axisymmetric, constant radius, dump combustor configuration (Fig. 3). Profiles of temperature, velocity, and soot volume fraction (soot volume fraction shown as a function of mixture fraction), computed by the joint pdf method, are compared in Figs. 4-7 for the following conditions: pressure, 10 atm, air temperature 917K, fuel temperature 478K, and equivalence ratio, 0.5. The predictions of the linear and non-linear models are seen to differ considerably, indicating that the net radiative loss and other flame properties may be sensitive to the choice of turbulence model. Also shown is the soot volume fraction derived from laminar flamelet data for a single value of strain rate. Since the absolute level of soot volume fraction is strain rate dependent the most significant finding in this comparison is that one effect of turbulence is to shift the peak volume fraction to leaner mixtures. More numerical examples will be given in the Subtask G discussion.



$$V_A = 50 \text{ m/sec}$$

$$V_F = 70 \text{ m/sec}$$

$$R_D = 0.122 \text{ m}$$

$$\phi = 0.5$$

Figure 3. Model dump combustor.

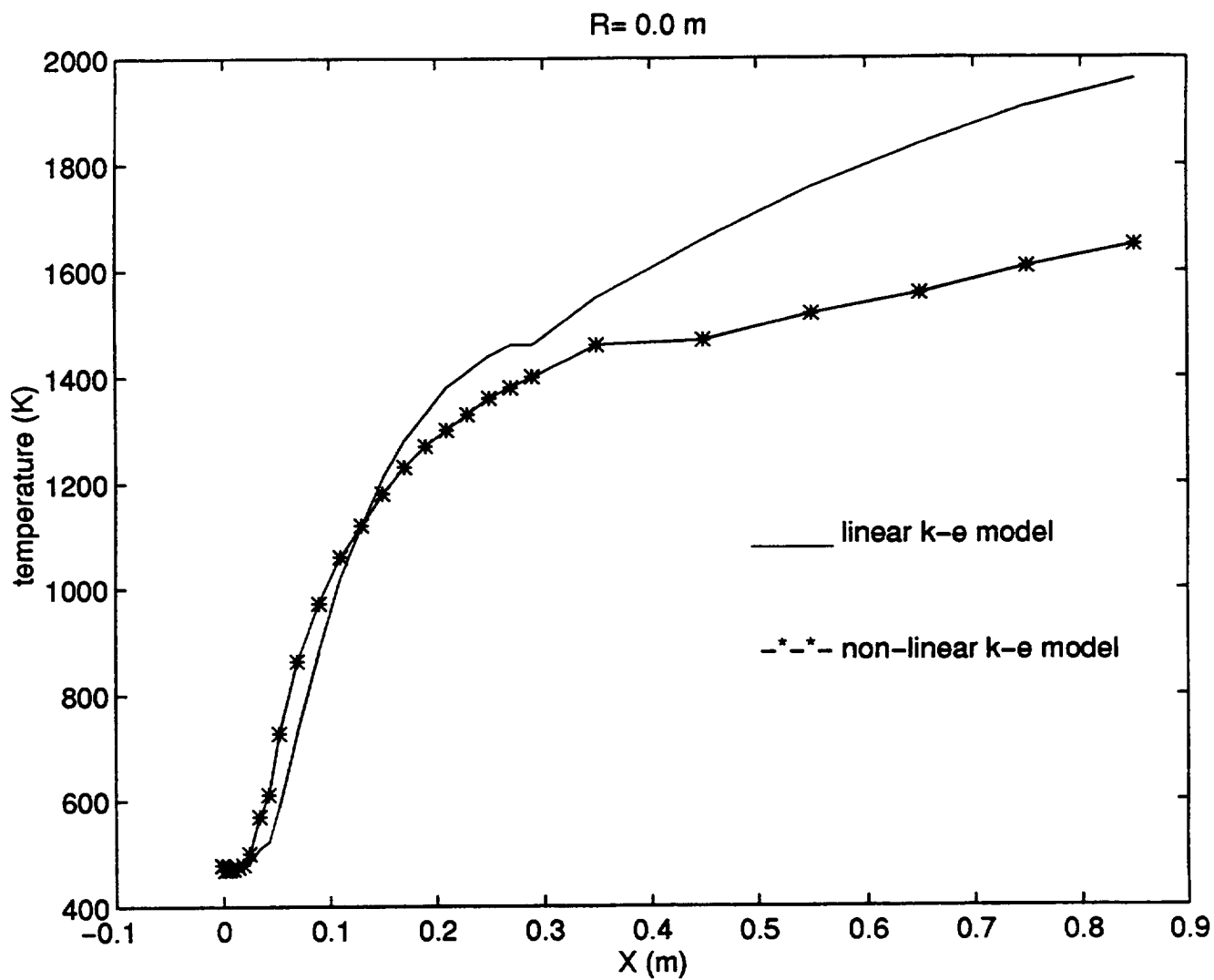


Figure 4. Comparison of centerline temperature profiles in TEACH code simulation.

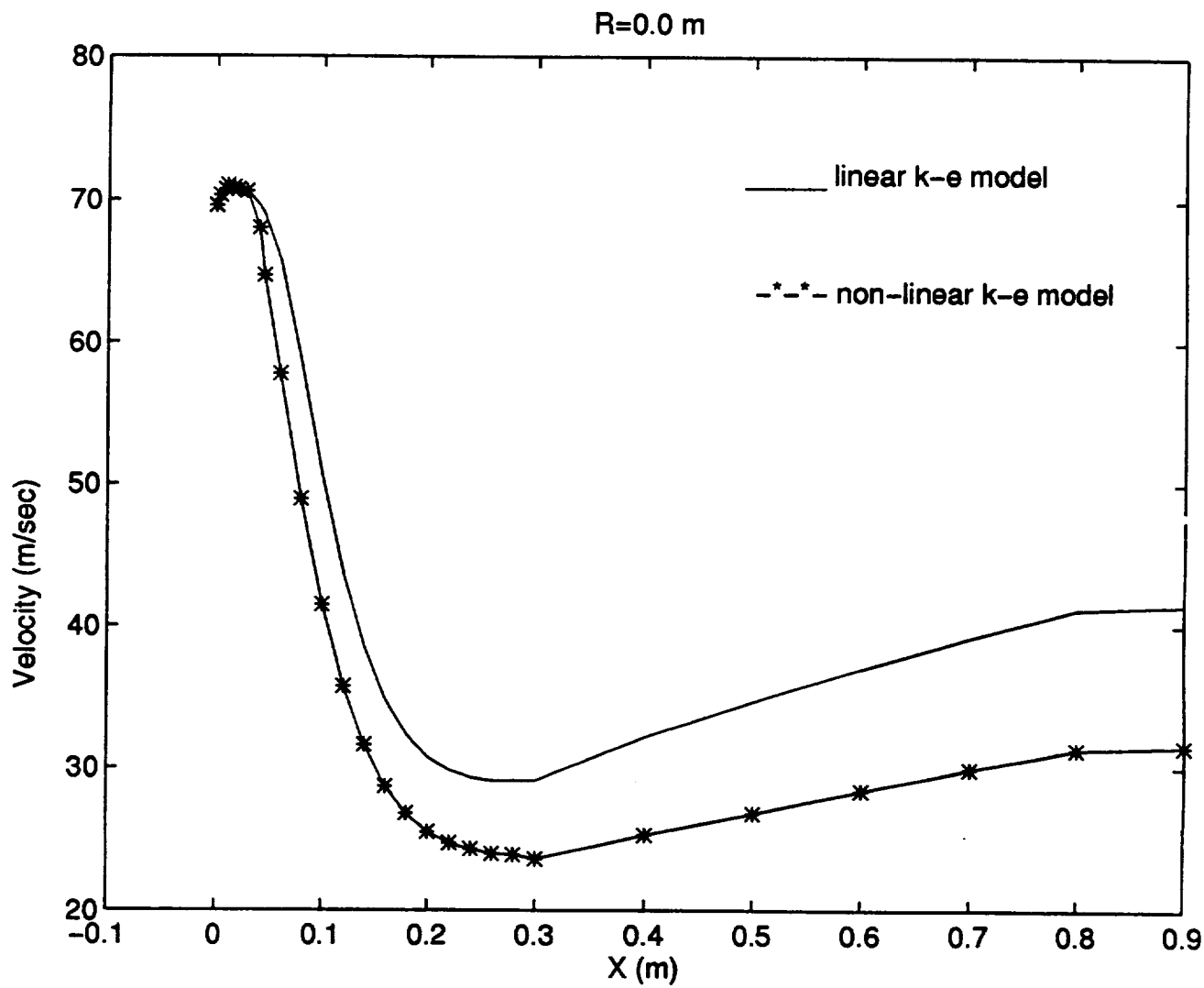


Figure 5. Comparison of centerline velocity profiles in TEACH code simulation.

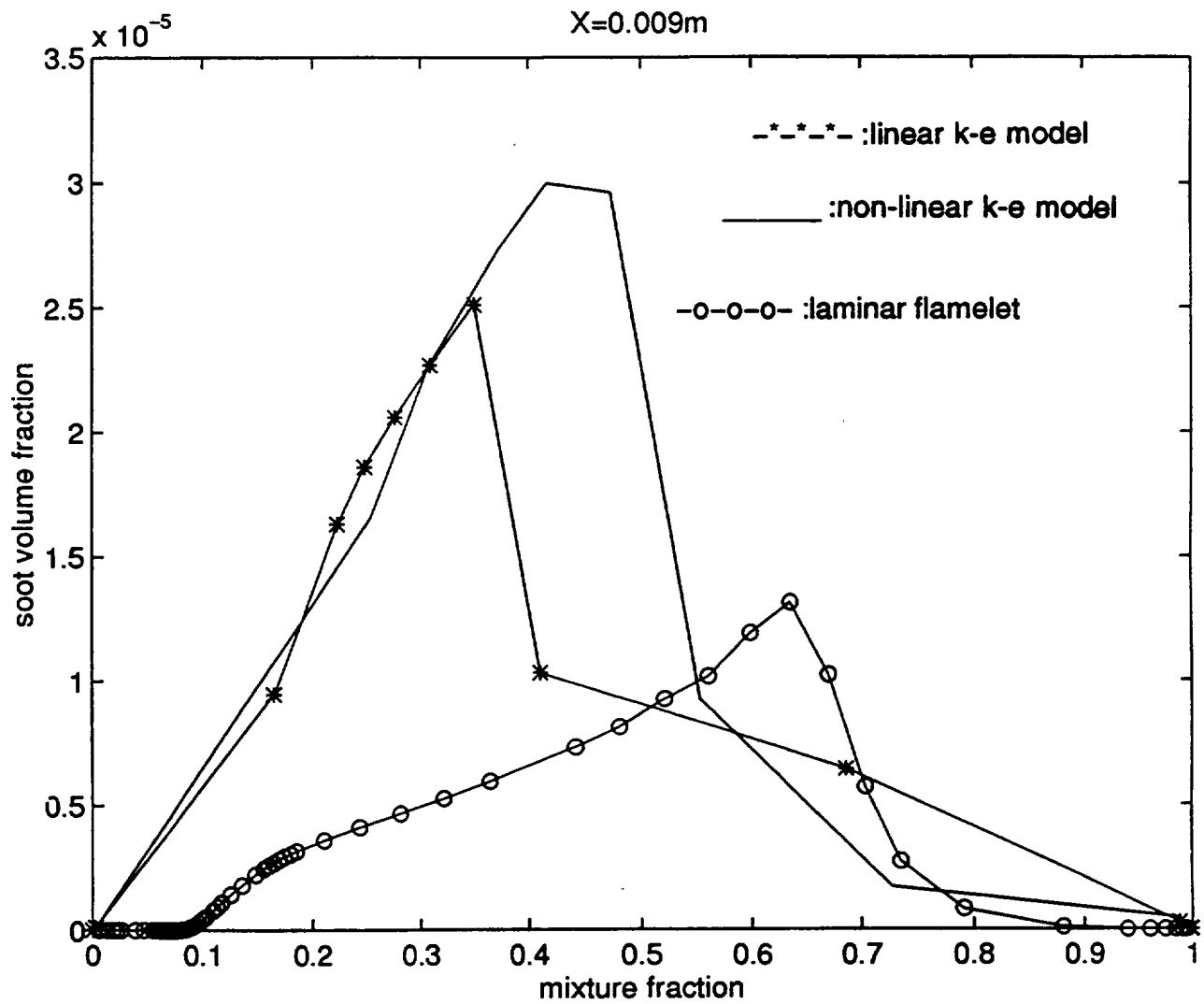


Figure 6. Joint pdf and laminar flamelet state relationships compared.

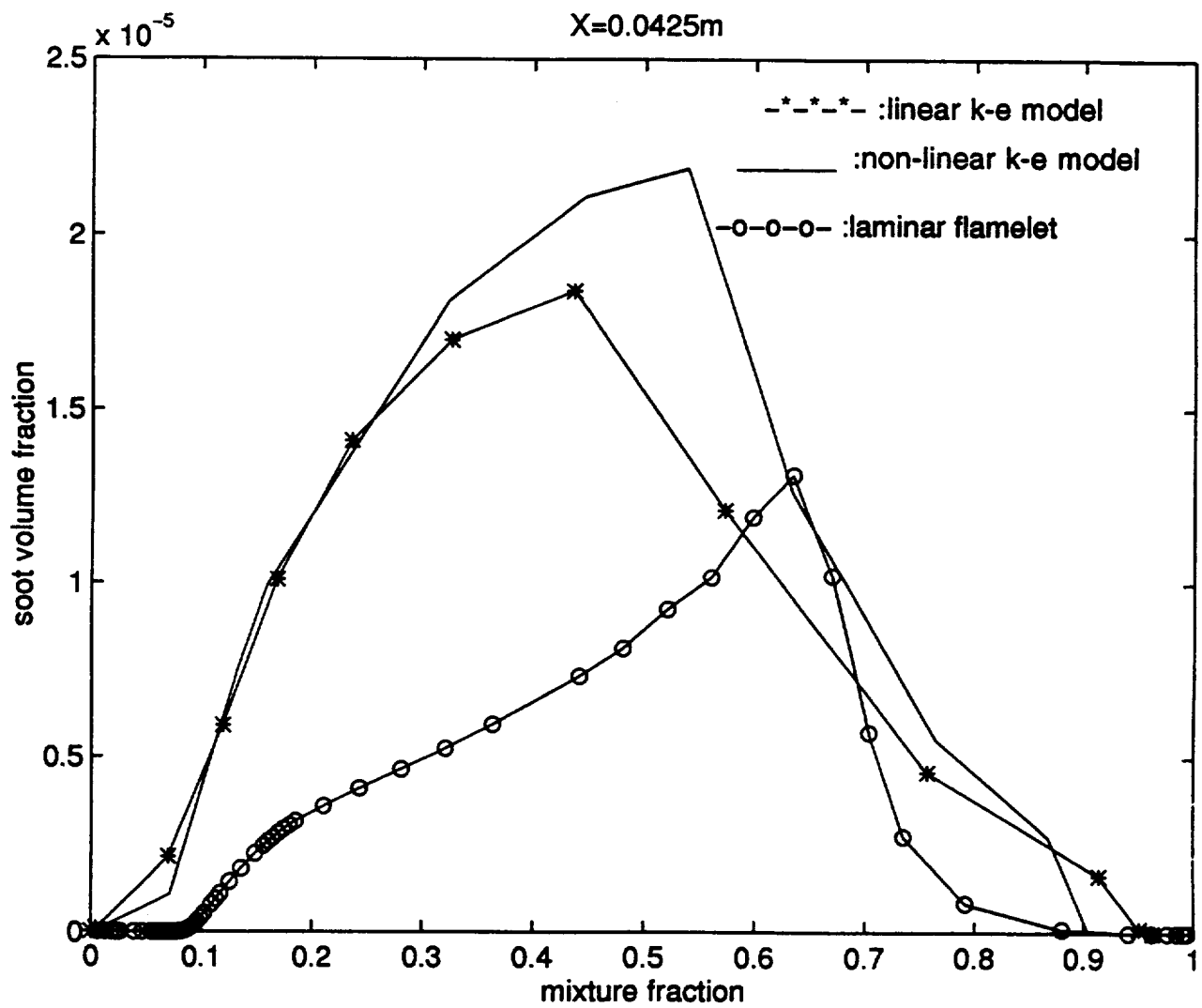


Figure 7. Joint pdf and laminar flamelet state relationships compared.

MODELING THE JOINT PDF

Mean flame properties are derived from underlying flamelet properties by statistical methods. The random variables involved in the averaging process are mixture fraction, z , scalar dissipation rate, χ , and a characteristic value of scalar dissipation rate which identifies a particular flamelet. The value at stoichiometric, χ_{st} , is usually chosen. χ and z are assumed to be statistically independent (Ref. 4). Experimental evidence indicates that z and χ are well represented by beta and lognormal probability density functions, $P(z; \alpha_i)$, and $P(\chi; \beta_i)$, respectively. α_i and β_i are each two parameter sets which complete the description of the probability densities. Three of the four parameters are described by transport equations which form part of the overall mean flow equation set. The remaining parameter (see Appendix B), related to the variance of χ , is experimentally derived and is assumed constant throughout the flow field. An expression for the joint probability density function is presented below.

Flamelet properties such as temperature, density, and composition are computed in the counter-flow flame calculation subject to imposed reactant flow rate boundary conditions which are related to χ_{st} . Individual flamelets are identified by their characteristic scalar dissipation rate χ_{st} . Any flamelet property $Q(z, \chi_{st})$ will then have a mean local value given by the following expression,

$$\langle Q \rangle = \int_0^\infty \int_0^1 Q(\chi_{st}, z) P(\chi_{st}, z) dz d\chi_{st} \quad (2)$$

where $P(\chi_{st}, z)$ is the joint density of z and χ_{st} .

The joint density is given by the expression (Ref. 4),

$$P(\chi_{st}, z) = f \cdot P_\chi(\chi_{st}f) \cdot P(z) \quad (3)$$

The shape factor f is defined as χ/χ_{st} and is found to be nearly independent of the flow rate boundary conditions. Thus, f is a function of z only.

The marginal density $P(\chi_{st})$, not used explicitly, but used as a check of the distribution function for χ_{st} , is obtained by integrating the joint density in z space. Thus,

$$P(\chi_{st}) = \int_0^1 P(\chi_{st}, z) dz \quad (4)$$

Numerical Integration

Since χ_{st} is unbounded it was necessary to assign an upper limit to χ_{st} , $\chi_{st \text{ max}}$, which yielded a value of the distribution function close to unity. The distribution function $F(\chi_{st})$ is defined by,

$$F(\chi_{st}) = \int_0^{\chi_{st}} P_{\chi_{st}}(\xi) d\xi \quad (5)$$

In principal, the distribution function could be evaluated at each point as a function of $\chi_{st \text{ max}}$ and $\chi_{st \text{ max}}$ chosen to satisfy some pre-determined value of the distribution function. This procedure would have been overly cumbersome, however, so an approximate procedure was used. An estimate of the standard deviation of χ_{st} was derived from analytical expressions for the moments of χ and assumptions of mean values of the shape factor $f(z)$. The upper limit of χ_{st} was then assumed to be three or four standard deviations above the mean value of χ_{st} . Occasional checks of the distribution function showed that an upper limit so defined was sufficiently large. Further details are given in Appendix B.

Subtask G. Soot Kinetics and Turbulent Radiation Model

This task, closely coupled to Subtask F, was comprised of the following:

1. Modification of a discrete transfer radiation code to provide for boundary-fitted coordinates in axisymmetric annular combustor geometries, and the inclusion of realistic, wavelength-dependent gas and soot radiative coefficients.
2. The inclusion of an efficient algorithm for turbulence effects on gas and soot radiation in the above code.
3. The prediction of soot growth in the model jet fuel flamelets at elevated pressure.
4. Coupling the output of the CFD solver and the sooting flamelet calculations to the radiation code.

TURBULENT RADIATION

Turbulent fluctuations enhance time-averaged radiation from flames relative to predictions based on time averaged flame properties, and the effect can be very large (Refs. 5-8). An analytic treatment of turbulence effects on monochromatic radiation was provided by Kabashnikov and Kmit (Ref. 5) for the Wien spectral regime and an assumed linear variation of absorption coefficient with gas temperature. Subsequent analysis of the effect in combustion has been mainly numerical in nature. The "Monte-Carlo" modelling approach of (Refs. 6,7) divides optical paths into a number of homogeneous, statistically independent elements with dimensions corresponding to the turbulence integral scale, and sets up possible instantaneous realizations of optical path. This has been done by randomly sampling the fuel mixture fraction distribution function within each homogeneous element, with the underlying pdf parameters derived from a turbulent flow model solution. Assumed state relationships between sampled mixture fraction and temperature/radiating species concentrations, usually taken from laminar flamelet solutions, complete the scheme. The inhomogeneous path

parameters are supplied as input to standard radiation band models, and the radiative intensity pdf is built up by performing many trials. This approach of setting up many realizations may not be practical in modelling complex combustor geometries with large numbers of grid points, however. The complexity of this approach has seemed so daunting that many modellers have been forced to neglect the effect in the hope that it is small in cases of interest to them. A simpler and faster semi-analytic approach for gas and soot radiation is described here, and found to give good agreement with the more cumbersome Monte-Carlo approach. It rests on the decorrelation of point- and path-averaged properties. A simpler calculation results in which attenuation-related terms are based on time averaged properties, and the local radiant power density is ensemble averaged over the fluctuation pdf using efficient numerical quadratures. Only one path integration, yielding the time-averaged intensity, is needed for the spectrally-integrated soot emission, and for each molecular band. The result is essentially equivalent to Monte-Carlo with a great reduction in computation time. The need to perform pdf averaging of the local radiant power density at each node point represents little more effort than is ordinarily expended in turbulent flow calculations where ensemble-averaged properties are desired. Numerical examples showing the application of this theory to a $\text{CH}_4\text{-H}_2$ turbulent diffusion flame and to a research combustor will be presented.

In the absence of scattering, and neglecting wall effects, line-of-sight monochromatic radiation can be represented by the integral

$$I = \int_0^s k(\omega, s') I_b(\omega, s') e^{-\int_{s'}^s k(\omega, s'') ds''} ds' \quad (6)$$

where k and I_b represent the local absorption coefficient and Planck function, respectively. For a fluctuating medium, the ensemble- or time-averaged intensity is represented by

$$\langle I \rangle = \int_0^s \langle k(\omega, s') I_b(\omega, s') e^{-\int_{s'}^s k(\omega, s'') ds''} \rangle ds' \quad (7)$$

Kabashnikov and Kmit suggested that under certain circumstances it suffices to replace the absorption coefficient in the attenuation term with its time average value, and to employ a time-averaged local power density at each point, e.g.

$$\langle I \rangle \simeq \int_0^s \langle k(\omega, s') I_b(\omega, s') \rangle e^{-\int_{s'}^s \langle k(\omega, s'') \rangle ds''} ds' \quad (8)$$

This is equivalent to saying that the time-averaged intensity is due mostly to fluctuations in the local emission power density, with the path-dependent exponential attenuation terms averaging out to some extent and making less of a contribution. The simplification afforded by this result is obvious, provided that something is known about the local turbulent fluctuation probability density. The only alternative is the inherently inefficient process of using random number generators to set up realizations of optical path, and building up the radiation statistics by performing a radiation calculation for each such realization. Hall and Vranos (Ref. 8,9) arrived independently at a similar conclusion for spectrally-integrated, wideband gas radiation. They verified their result for turbulent diffusion flame radiation by comparisons with such "Monte Carlo" calculations. (In this paper, Monte Carlo will be used in a somewhat different sense than it usually is in radiation calculations). Kabashnikov and Kmit, and Krebs, et al (Ref. 10) have shown that a condition for the validity of this approach is that individual eddies not be optically thick. For soot radiation, this condition will usually be satisfied. For the CO₂ 4.3 μ band, there may be violation at high pressures, but usually the soot radiation will be dominating. The application to gas and soot radiation in combustors will now be discussed.

GAS RADIATION

The analysis of turbulent gas radiation has been given by Hall and Vranos using the exponential wideband model (Refs. 8, 9, 11). It will be illustrated by application to a turbulent diffusion flame. With the usual simplification that the absorption features vary much more rapidly than the Planck function, the intensity generated along a line of sight can be represented as

$$I = \sum_i \int_0^s \frac{dA_i}{ds'} I_b(\omega_i^{(0)}, s') ds' \quad (9)$$

where I_b is the Planck function evaluated at band center frequency $\omega_i^{(0)}$, and the subscript i denotes the i -th active molecular band. Here A_i is the integrated band absorptance, which for combustion problems can be well approximated using the high pressure form

$$\frac{A}{\Delta\omega} = (\ln(\xi/\Delta\omega) + E_1(\xi/\Delta\omega) + \gamma_E) \quad (10)$$

$$\xi = \alpha \rho |s - s'|$$

where $\Delta\omega$ is molecular resonance bandwidth, α is integrated band intensity, and ρ is the infrared active species density. Band overlaps are neglected, and it is understood that a summation over all active bands of H_2O , CO_2 , and CO will be performed to calculate intensity. Neglecting band overlap effects, the subscript can be suppressed with the understanding that a sum over all bands will be performed at the end.

There is much current discussion in the radiative transfer community about the relative merits of narrowband, wideband, and line-by-line calculations (Ref. 12). The latter are too time consuming for practical applications at the present time, and narrowband models are thought to be more accurate than the wideband. However, for engineering purposes the computationally efficient wideband models are felt to be acceptable (Ref. 13), particularly since soot radiation will be dominant in most cases of interest. As will be seen in the next section, the calculation of soot radiation is more nearly exact, requiring none of the approximations that are inherent in the band models.

For nonhomogeneous optical paths, the Curtis-Godson scaling approximation as given by Morizumi and Edwards (Ref. 14) is employed. In this approximation, the band absorptance is expressed in terms of scaled parameters as

$$\frac{A}{\Delta\omega} = \ln(\xi/\Delta\bar{\omega}) + E_1(\xi/\Delta\bar{\omega}) + \gamma_E \quad (11)$$

where

$$\xi = \int_{s'}^s \alpha \rho \, ds'' \quad (12)$$

$$\overline{\Delta\omega} = \frac{1}{\xi} \int_{s'}^s \omega \rho \alpha \, ds'' \quad (13)$$

Thus, we have, approximately,

$$I \simeq \int_0^s \left(\frac{\overline{\Delta\omega}}{\xi} \right) (1 - e^{-\xi/\overline{\Delta\omega}}) \rho \alpha I_b \, ds' \quad (14)$$

The quantity of interest is the ensemble average of Eq. 14. In the integrand, the factor $\rho \alpha I_b$ is point specific, but multiplies an A-derivative factor that involves only path averaged properties, as per Eqs. 11-13. Inasmuch as these paths traverse eddies or volume elements that are presumed to be statistically independent, one can make the approximation that the two factors in the integrand are statistically independent, i.e.

$$\langle I \rangle = \int_0^s \left\langle \frac{\overline{\Delta\omega}}{\xi} (1 - e^{-\xi/\overline{\Delta\omega}}) \right\rangle \langle \rho \alpha I_b \rangle \, ds' \quad (15)$$

where $\langle \rangle$ denotes ensemble- or time-averaging.

It will be assumed that state relationships giving temperature T and species densities in terms of the fuel mixture fraction pertain. These are obtained in laminar flamelet theory from opposed jet solutions at a representative value of strain rate; typically the radiating gas species concentrations and temperature are not strongly sensitive to strain rate if the strain rate is in the appropriate range. Thus, if the probability density $p(z, \eta_i)$ for mixture fraction z is known, where η_i are the known parameters of the pdf, the ensemble average

$$\langle \rho \propto I_b \rangle = \int_0^1 p(z; \eta_i) \rho(z) \alpha(T(z)) I_b(T(m)) dz \quad (16)$$

can be regarded as a known quantity at each point along the optical path. The crux of the analysis lies in showing that the ensemble average of the other function of path- averaged properties is adequately represented by evaluation of the function with time-averaged properties, i.e.

$$\left\langle \frac{\overline{\Delta\omega}}{\xi} (1 - e^{-\xi/\Delta\bar{\omega}}) \right\rangle \simeq \frac{\langle \overline{\Delta\omega} \rangle}{\langle \xi \rangle} (1 - e^{-\langle \xi \rangle / \langle \Delta\bar{\omega} \rangle}) \quad (17)$$

where the terms on the r.h.s. are evaluated on the basis of time- averaged properties. Details are given by Hall and Vranos.

Example calculations are now shown for an atmospheric pressure, $\text{CH}_4\text{-H}_2$ turbulent diffusion flame on which extensive diagnostic measurements have been reported in Ref. 15. The flowfield was simulated with a standard $k\text{-}\epsilon$ turbulence model and a parabolic flow solver, providing at each spatial node point the mean fuel mixture fraction and its variance. We assume for these example calculations that the mixture fraction pdf $p(z)$ is described by the beta density (Ref. 16),

$$\begin{aligned} p(z) &= \frac{\Gamma(a+b)}{\Gamma(a)\Gamma(b)} z^{a-1} (1-z)^{b-1} \\ a &= \gamma \langle z \rangle \\ b &= \gamma (1 - \langle z \rangle) \\ a+b &= \gamma \\ \gamma &= \frac{\langle z \rangle (1 - \langle z \rangle)}{\langle z'^2 \rangle} - 1 \end{aligned} \quad (18)$$

where Γ is the gamma function, and $\langle z \rangle$ and $\langle z'^2 \rangle$ are the mixture fraction mean and variance, respectively. The state relationship between mixture fraction and temperature, density, and species concentrations was assumed to be given by an opposed jet or counterflow flame solution, employing a widely used program (Ref. 17). Mixture fraction is here defined as the average of the C- and

H-atom mixture fractions, each of which has been normalized to its fuel side value. These solutions are characterized by a representative value of the strain rate, roughly the velocity gradient normal to the flame structure, and a solution corresponding to a median value is used. When soot is included in the flamelet calculations, the joint pdf of z and scalar dissipation (strain rate) must be employed, as has been discussed in Subtask F. The $k-\epsilon$ based parabolic code gives a solution in distances normalized by the inner fuel tube radius (Figure 8). The optical paths were divided into segments of length corresponding to the local integral scale. The "Monte Carlo" calculations were then performed in a way similar to Refs. 6, 7. Within each independent volume element, a random number generator was used to randomly sample the mixture fraction distribution function (Ref. 6). From the resulting value of mixture fraction the instantaneous temperature and species concentrations were then interpolated from the opposed jet state relationships. The intensity for the realization was then calculated from Eqs. 15-17, summing the active bands. It is also possible to make a calculation of radiative flux based on time-averaged temperature and density. The quantity of interest is the ratio of time-averaged intensity to intensity based on time-averaged properties, or the intensity enhancement.

Table 2 compares the "Monte Carlo" and "analytic" predictions for the time-averaged, line-of-sight intensity at two heights above the burner surface. The two heights encompass a significant range of optical thickness, as shown by the band center optical depth of the H_2O 6.3μ transition. As seen, the "analytic" predictions, which are much more efficiently obtained, satisfactorily agree with the Monte Carlo predictions. There are minor differences, not shown, in the absolute value of predicted mean properties having to do with the much different algorithms for the two types of calculations. This gas band discussion has employed wideband models. If the use of narrowband models is preferred, there seems little reason to believe that the underlying result would not be applicable to them, as well.

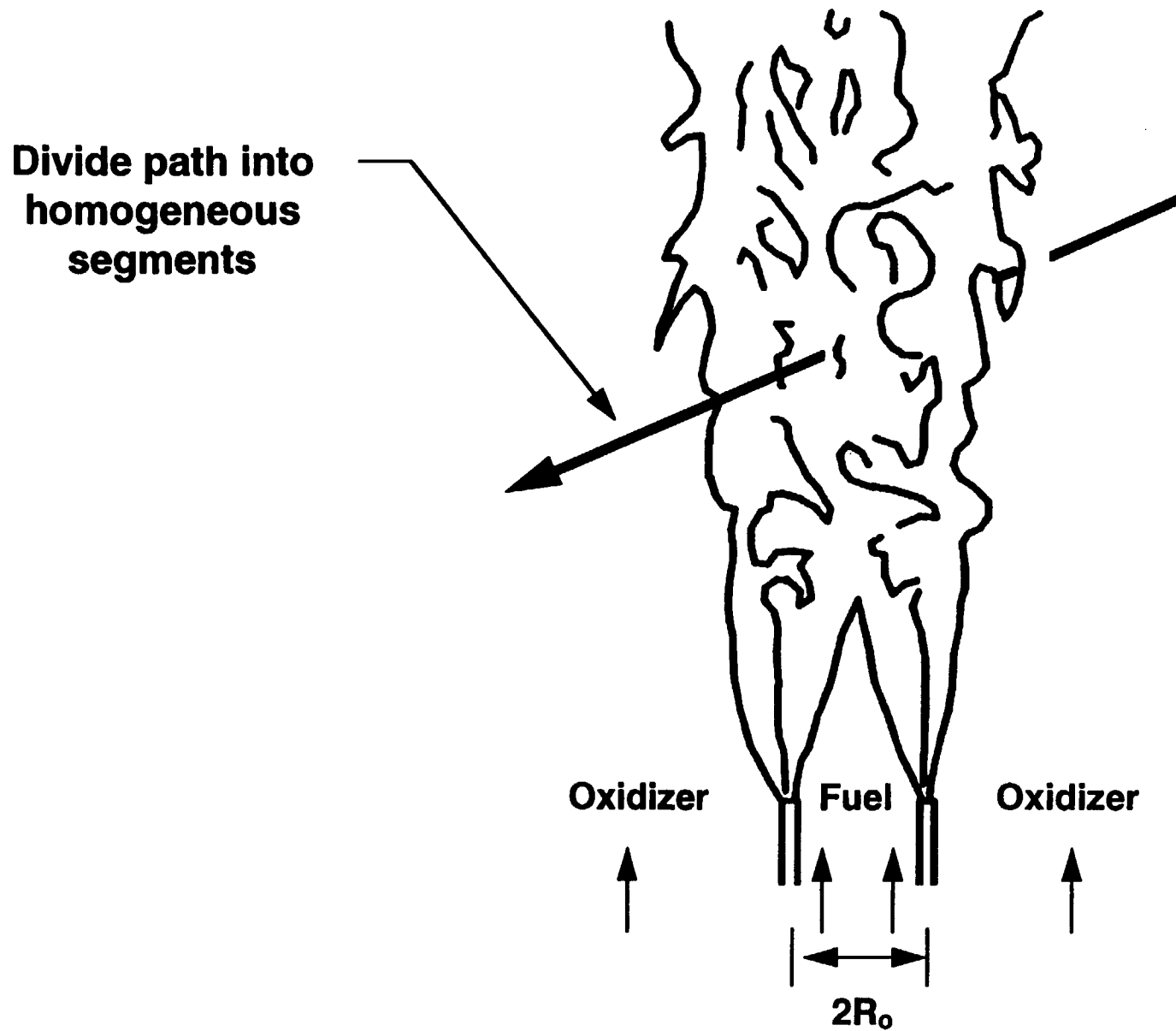


Figure 8. Representation of turbulent diffusion flame showing division of optical path for radiation calculations into statistically independent segments.

Table 2

Intensity Enhancement Factors - $\frac{\langle I \rangle}{I(\langle T \rangle)}$

H (cm)	"Monte Carlo"	"Analytic"	$(\xi/\Delta\omega)_{6.3\mu}$
25	1.317	1.327	0.73
200	1.194	1.197	2.54

SOOT RADIATION AND DISCRETE TRANSFER ANALYSIS

The discussion of turbulent soot radiation is illustrated with an application to a realistic combustor geometry. A flux model for axisymmetric, annular geometries has been developed using the discrete transfer model of Lockwood and Shah (Refs. 18, 19). The discrete transfer algorithm has been selected because it gives considerable geometric flexibility, as is well known. A boundary-fitted coordinate system that uses transfinite interpolation is employed, so that curved inner and outer radial boundaries can be handled. Application of the program to a simulated annular combustor geometry is shown in Figure 9. The program works its way around the boundaries of the combustor, at each point P firing rays in all directions into the combustor, and locating the points of intersections with the walls. These wall intersection points serve as starting points for line-of-sight radiation calculations back to the point P, at which the net radiative flux is calculated. The x symbols denote the points at which the rays pass through axial and radial boundaries; for each ray, a list of the cells passed through and the length of the ray within each cell is made for the radiation calculation. Because medium properties will vary from cell to cell, this allows medium inhomogeneities to be accounted for. The grid should be fine enough to resolve the gradients in average temperature; if the turbulent radiation algorithm is to be applied, it is important that the properties in adjacent cells be statistically independent. The rays which seem to be highly curved correspond to paths emanating from the outer radial wall, miss the inner radial wall, and end in the outer wall. The radiative flux divergences (from which gas cooling rates can be derived) can also

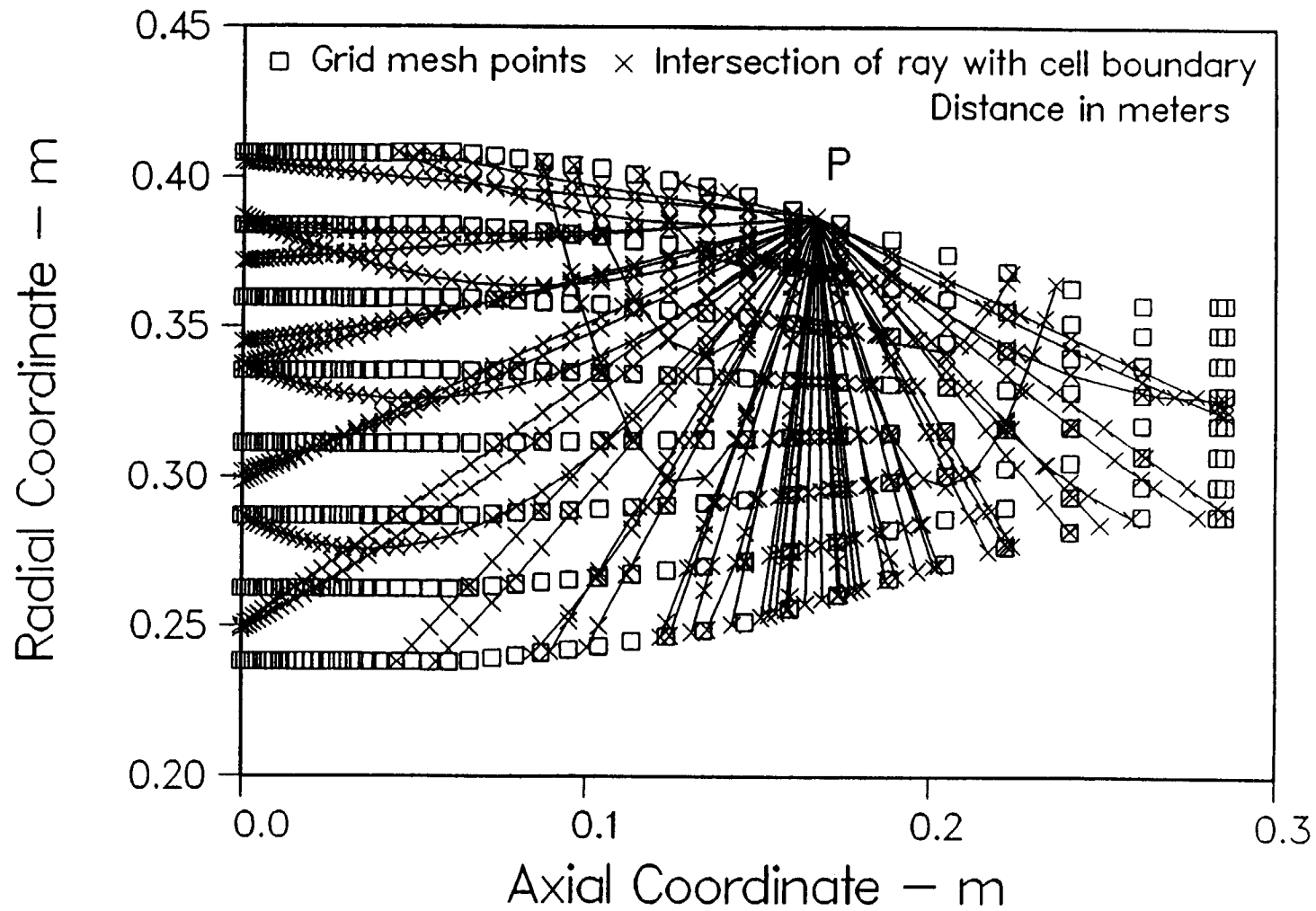


Figure 9. Discrete transfer rays in model, axisymmetric annular combustor.

be calculated for each cell; to do so requires calculation of the internal radiative intensities. Wall fluxes tend to become relatively insensitive to the number of rays at around 32 rays per point per quadrant; depending on the geometry and mesh, however, larger numbers of rays may be needed to sample certain remote cells for accurate radiative dissipation calculations in these cells. The line-of-sight radiation calculations can be performed either with a narrowband radiation model (Ref. 20), or with a combination of the wideband gas model discussed in the last section and a quasi-analytic soot model which will now be discussed.

The calculation of spectrally-integrated soot radiation along a homogeneous path can be represented in closed form if gas radiation effects are small. Given typical thermal radiation wavelengths, soot particles are usually in the small size parameter or Rayleigh range where scattering is negligible. To first order, if intracluster multiple scattering effects are small, the soot absorption coefficient can be taken to have the form appropriate to Rayleigh spheroids even for clusters, e.g.

$$k_s(\omega) = c_s \omega f_v \quad (19)$$

where f_v is the particle volume fraction, ω in units cm^{-1} , and the constant c_s is related to the complex soot index of refraction. It will be convenient to ignore both the frequency dispersion of c_s and its temperature dependence. If the Planck function is represented as

$$I_b(T) = c_1 \omega^3 \sum_{n=1}^{\infty} e^{-nc_2 \omega/T} \quad (20)$$

line-of-sight soot radiation can be represented by the double integral over path and frequency

$$I = c_s c_1 \int_0^s ds' \int_0^{\infty} d\omega \omega^4 \sum_{n=1}^{\infty} e^{-\frac{n\omega c_2}{T(s')}} f_v(s') e^{-c_s \omega \int_{s'}^s f_v(s'') ds''} \quad (21)$$

the frequency integral can be done first, using

$$\int_0^{\infty} \omega^4 e^{-a\omega} d\omega = 4!/a^5 \quad (22)$$

giving

$$I = 4!c_s c_1 \sum_{n=1}^{\infty} \int_0^s \frac{f_v(s') ds'}{(nc_2/T(s') + c_s \int_{s'}^s f_v(s'') ds'')^5} \quad (23)$$

which is equivalent to, for a homogeneous path,

$$I = 3!c_1 \sum_{n=1}^{\infty} \left(\frac{1}{(nc_2/T)^4} - \frac{1}{(nc_2/T + c_s f_v s)^4} \right) \quad (24)$$

If the optical path is inhomogeneous (Figure 10), the intensity line integral, Equation 21, can be represented as a sum of N terms over each of which the path integral can be done analytically, as in Equation 24. This gives the inhomogeneous path expression

$$\begin{aligned} I = 3!c_1 \sum_{n=1}^{\infty} & \left(\frac{1}{(nc_2/T_1)^4} - \frac{1}{(nc_2/T_1 + c_s f_v(1)\Delta_1)^4} \right. \\ & + \frac{1}{(nc_2/T_2 + c_s f_v(1)\Delta(1))^4} - \frac{1}{(nc_2/T_2 + c_s (f_v(1)\Delta(1) + f_v(2)\Delta(2)))^4} \\ & + \frac{1}{(nc_2/T_3 + c_s (f_v(1)\Delta(1) + f_v(2)\Delta(2)))^4} - \frac{1}{(nc_2/T_3 + c_s (f_v(1)\Delta(1) + f_v(2)\Delta(2) + f_v(3)\Delta(3)))^4} \\ & \left. + \dots \frac{1}{(nc_2/T_N + c_s F_{N-1})^4} - \frac{1}{(nc_2/T_N + c_s F_N)^4} \right) \end{aligned} \quad (25)$$

where

$$F_i = \sum_{j=1}^i f_v(j)\Delta(j)$$

A wall at Q with temperature T_w will add to Equation (25) the expression

$$I_w = 3!\epsilon_w c_1 \sum_{n=1}^{\infty} \frac{1}{(nc_2/T_w + c_s F_N)^4} \quad (26)$$

If the wall is non-black, and we can assign an effective radiation temperature T_r to the flux incident on Q, Equation (26) can be replaced by

$$S = \sum_{j=1}^N \Delta_j$$

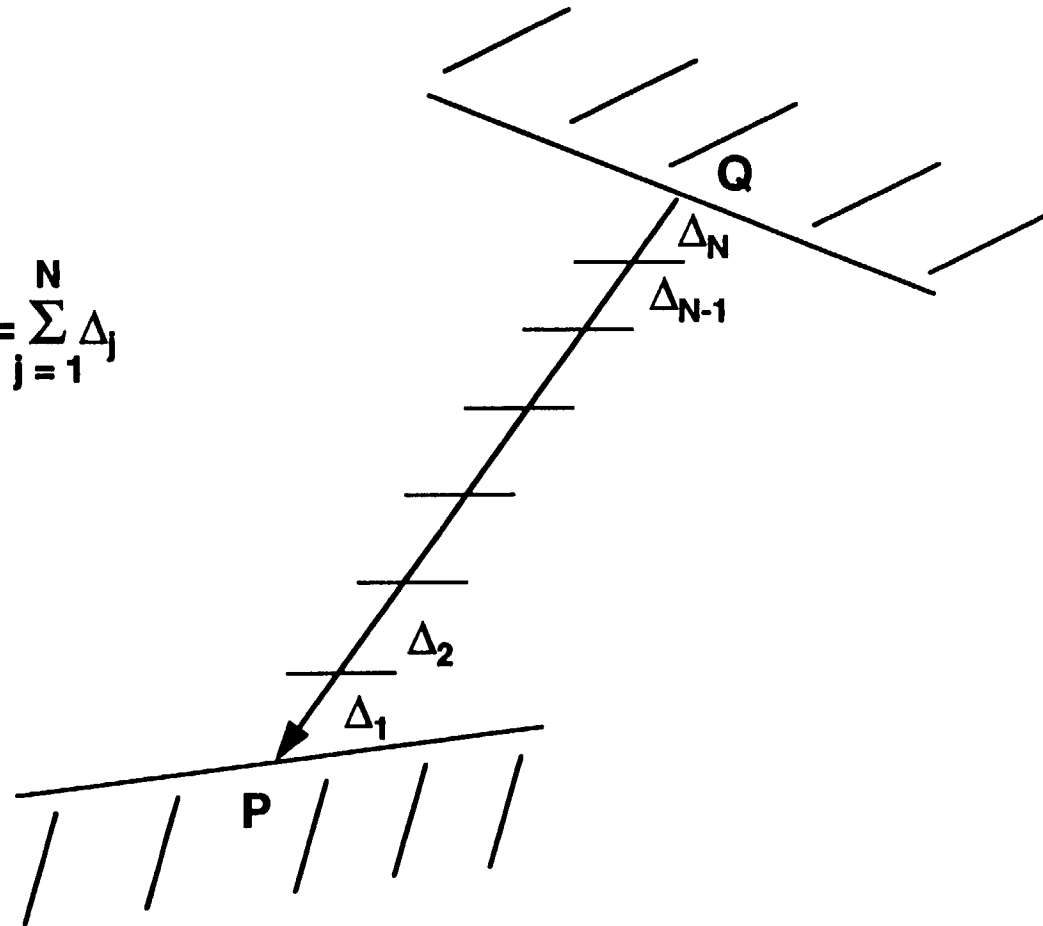


Figure 10. Representation of discrete transfer optical path for analytic soot radiation analysis.

$$I_w = I_w \text{ (Eq. 26)} + 3!(1 - \epsilon_w)c_1 \sum_{n=1}^{\infty} \frac{1}{(nc_2/T_r + c_s F_N)^4} \quad (27)$$

as the contribution of the opposite wall to the radiation at P.

Radiation fluxes calculated using Eqs. 25-27 agree precisely with those using the narrowband RADCAL representation (Ref. 20) provided that a consistent value of c_s is used (assumed equal to 7.0 for c.g.s wavelengths). In the Eqs. 25-27 calculation the frequency summation is done analytically as shown; in the narrowband calculation it is done numerically, thus giving rise to considerable efficiency enhancement in the former case. A sample comparison is shown in Figure 11 for the outer annular wall of the model combustor shown in Figure 9. A uniform temperature of 2000 K and uniform volume fraction of 10^{-6} and cold, black walls have been assumed. The agreement is also exact for inhomogeneous medium test cases.

To calculate soot radiation from turbulent flames, the stochastic analysis requires that $f_v(s')$ in the integrand of Equation 21 be decorrelated from the path integral of volume fraction appearing as the exponential argument in the integrand. Doing so (but keeping the correlation of $f_v(1)$ with the path integral for $\Delta(1)$) gives

$$\begin{aligned} \langle I \rangle = & 3!c_1 \sum_{n=1}^{\infty} \left\langle \frac{1}{(nc_2/T_1)^4} - \frac{1}{(nc_2/T_1 + c_s f_v(1)\Delta(1))^4} \right. \\ & + \frac{f_v(2)}{\langle f_v(2) \rangle} \left(\frac{1}{(nc_2/T_2 + c_s \langle f_v(1) \rangle \Delta(1))^4} - \frac{1}{(nc_2/T_2 + c_s (\langle f_v(1) \rangle \Delta(1) + \langle f_v(2) \rangle \Delta(2)))^4} \right) \\ & \dots + \frac{f_v(N)}{\langle f_v(N) \rangle} \left(\frac{1}{nc_2/T_N + c_s \langle F_{N-1} \rangle^4} - \frac{1}{(nc_2/T_N + c_s \langle F_N \rangle)^4} \right) \Bigg\rangle \end{aligned} \quad (28)$$

with

$$\langle F_i \rangle = \sum_{j=1}^i \langle f_v(j) \rangle \Delta(j)$$

where the T_i and the $f_v(i)$ are fluctuating quantities.

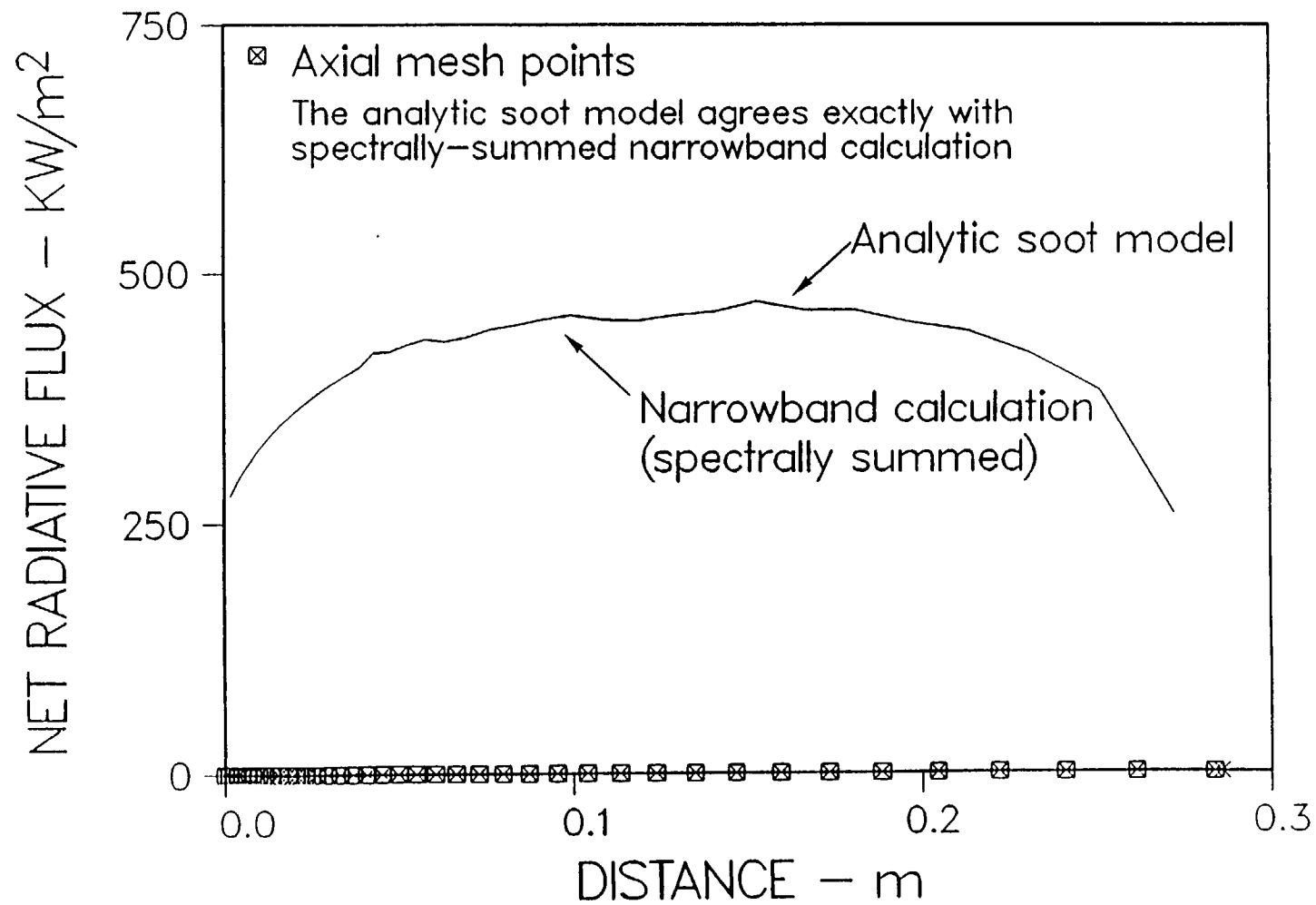


Figure 11. Net radiative flux along outer radial surface in Figure 9 model combustor.

This has the following limits

Optically thick

$$\langle I \rangle \Rightarrow 3!c_1c_2^{-4} \langle T_1^4 \rangle \sum_{n=1}^{\infty} \frac{1}{n^4} = \frac{\sigma}{\pi} \langle T_1^4 \rangle \quad (29)$$

Optically thin

$$\langle I \rangle \Rightarrow 4!c_1c_2^{-5} \sum_{n=1}^{\infty} \frac{1}{n^5} \sum_{i=1}^N \langle f_v(i) T_i^5 \rangle \Delta(i) \quad (30)$$

In the optically thick limit, the time-averaged flux loses its sensitivity to fluctuations in volume fraction, and becomes proportional to the time-averaged value of T^4 at the wall. Wall contributions, Eqns. 26, 27 will be evaluated on the basis of average soot volume fraction and the time-averaged T_r .

Discrete transfer calculations for an annular combustor shape representative of the RQL rich zone are shown in Figures 12 and 13. For the homogeneous temperature and volume fraction values chosen, the net radiative fluxes on the inner and outer radial surfaces (assumed to be cold and black) are shown. The outer wall sees more radiating gas and has higher predicted fluxes. On both surfaces, the contraction is predicted to be an area of high flux because the surface normal is exposed to a longer optical path.

COMBINED GAS AND SOOT RADIATION

The combined effect of gas and soot radiation is not simply additive, mainly because of absorption of gas band radiation by the soot continuum. The gas bands also absorb soot radiation to some degree. Each gas band's radiation is attenuated by the soot absorption coefficient at the band center frequency. Thus, Eq. 9 becomes

$$I = \sum_i \int_0^s e^{-c_i \omega_i^{(0)} \int_{s'}^s f_v(s'') ds''} \frac{dA_i}{ds'} I_b(\omega_i^{(0)}, s') ds' \quad (31)$$

where the i summation extends over all molecular bands.

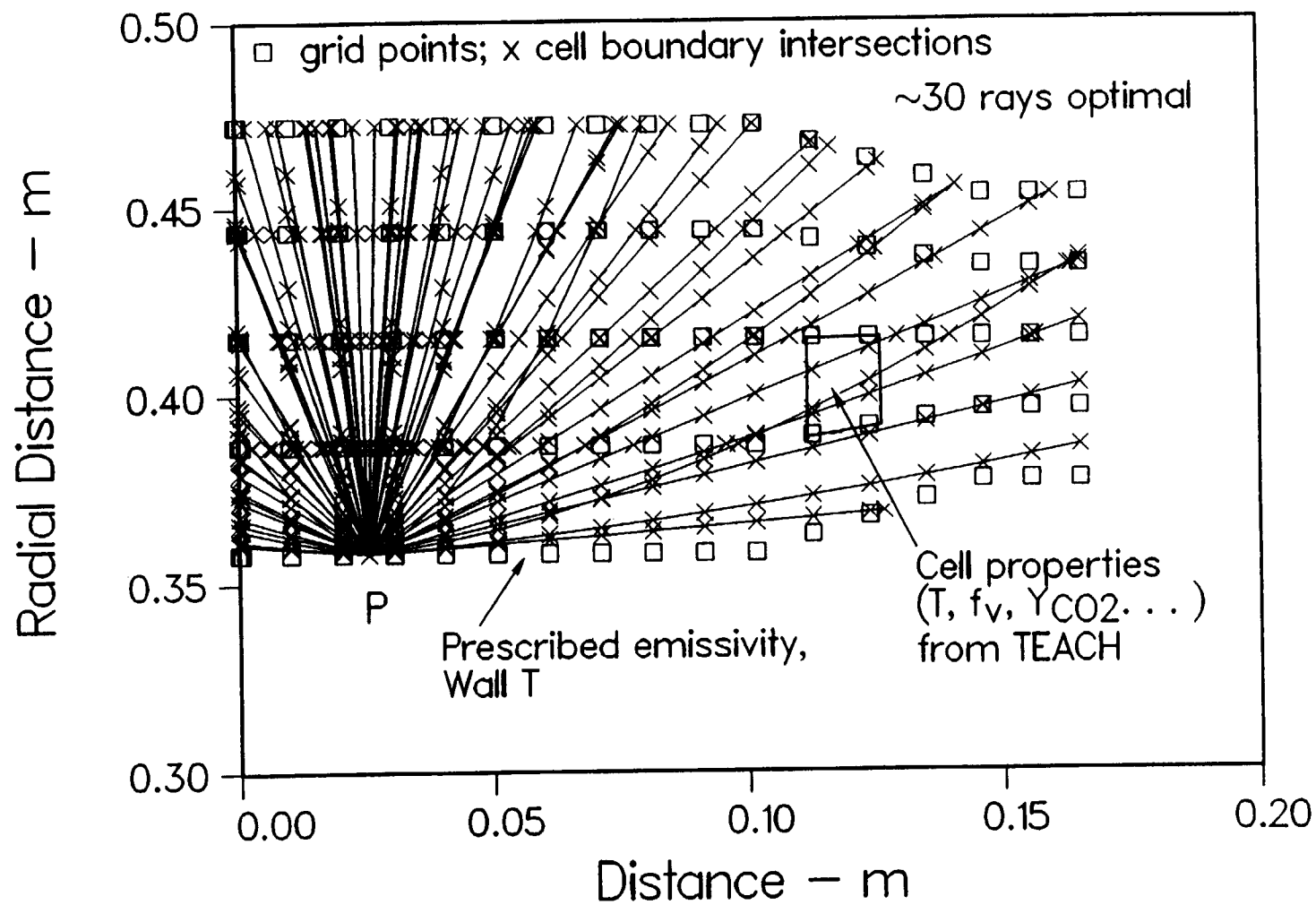


Figure 12. Discrete transfer analysis of RQL rich zone.

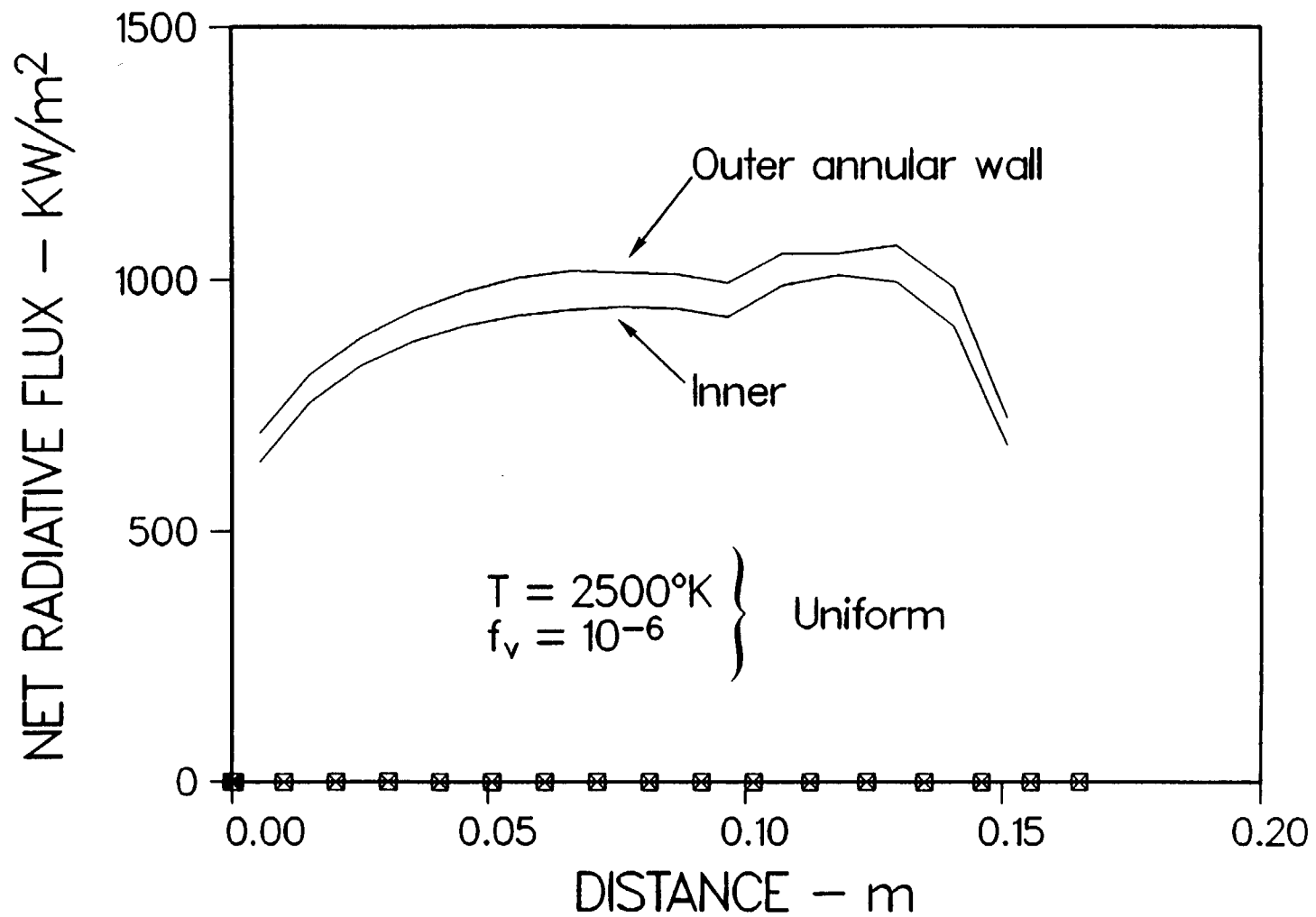


Figure 13. Net radiative fluxes on RQL inner and outer radial walls.

The absorption of soot continuum radiation by the gas bands employs an approximation given in Ref. 21. The total soot radiation is Equation 25 plus the expression

$$c_s \sum_i \omega_i^{(0)} \int_0^s ds' f_v I_{bi} \overline{\Delta\omega_i} \left[e^{-(\tau_s^{(i)} + \xi_i/\overline{\Delta\omega_i})} - e^{-\tau_s^{(i)}} \right] \quad (32)$$

where $\tau_s^{(i)} = c_s \omega_i^{(0)} \int_{s'}^s f_v ds''$; ξ_i and $\overline{\Delta\omega_i}$ are as defined in Equation 7 and 8, and $I_{bi} = I_b(\omega_i^{(0)})$.

Thus, the total radiative flux when both gas and soot are present is given by Equations 25, 31 and 32. In turbulent media, the soot and radiation follows the previously discusses treatments, but the soot attenuation term in Equation 31 and the entire Equation 32 are based on time-averaged properties. This treatment of gas-soot overlap effects is not exact, but its predictions are generally close enough to those based on more exact narrowband calculations to be acceptable for engineering purposes.

Soot scattering has been ignored in this analysis beacause typical soot sizes of 0.05 to 0.1 micron and the wavelengths of interest in thermal radiation analysis produce relatively small size parameters ($\pi D/\lambda$) that are associated with weak Rayleigh scattering. The large imaginary part of the soot index of refraction also dictates that the soot extinction is largely due to absorption. Scattering could, however, be included if unusually large soot particles were predicted or observed.

SOOT DISTRIBUTIONS IN MODEL JET FUEL FLAMELETS

As discussed, the microflow for the stretched flamelet/pdf approach to turbulence modelling is the counterflow flame, depicted in Figure 14. The soot concentrations for the model jet fuel flamelets were calculated using an opposed jet solver with complex chemistry that has had added to it the dynamical and transport equations of soot spheroid growth (Ref. 22). The modular spheroid dynamical model includes inception, coalescence, surface growth, and oxidation, and uses the sectional or size bin representation. The model also accounts for soot particle scrubbing of growth species and oxidants, and for gas and soot radiation. Before this model could be applied

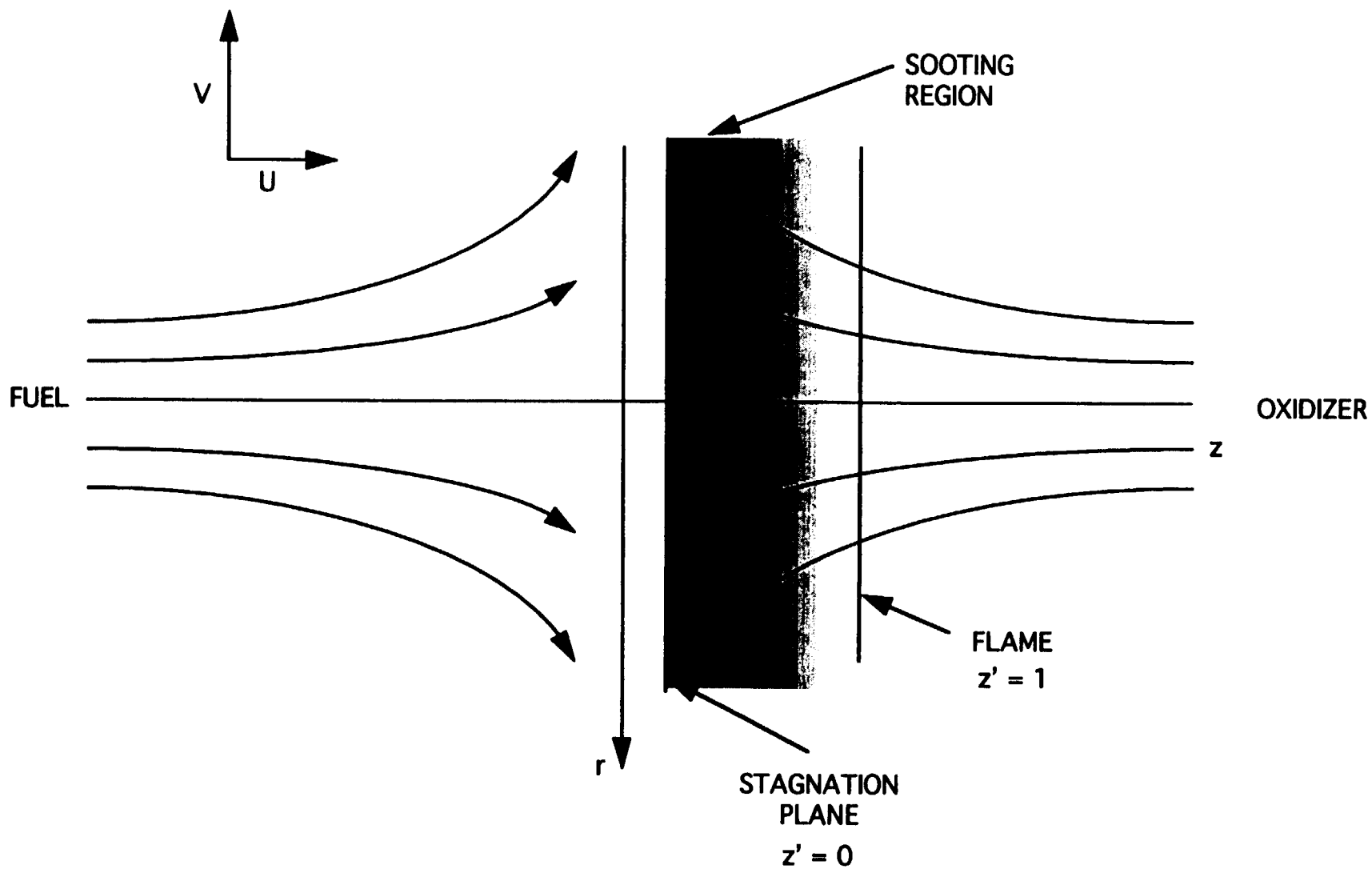


Figure 14. Configuration of opposed jet, laminar diffusion flame.

to the present problem, however, a number of code enhancements had to be carried out. The first was the creation of a potential flow version more appropriate for flamelet calculations than the plug flow assumption used in the original program. Second, since high pressure calculations were desired, pressure effects on the soot growth kinetics had to be included. As pressure increases, the largest particles move from the free-molecule growth regime (mean free path larger than particle size) to the so-called continuum regime. Correction for this effect is non-trivial, and certain of the needed code modifications were carried out on this contract. The main correction made was to correct the particle coalescence frequencies for continuum effects. This has a pronounced effect for pressure levels on the order of ten atmospheres, and it is felt that the corrections made are adequate for moderate pressures. To extend the calculations to much higher pressures, however, further corrections to the thermophoretic velocities and the surface growth expression would be required.

The model jet fuel kinetics mechanism had 42 species and 123 chemical reactions (Appendix A). The soot volume fraction is generally insensitive to the number of size bins, but accurate average soot size and number require more bins. A compromise of eight bins was employed in these calculations. Volume fraction is the soot size/density parameter of most interest for radiation calculations. The major uncertainties in soot loading calculations are associated with the modelling of the nucleation and surface growth processes. The field of soot growth modelling is being actively investigated, and answers to these questions are being refined. For these calculations, a relatively simple, but widely used and highly successful model due to Lindstedt and co-workers (Ref. 23) has been used. While developed for methane, it has been applied with good results in many simulations, one of the most noteworthy being in co-flow, acetylene-air diffusion flames (Ref. 24). In this model, both inception and surface growth are proportional to acetylene concentration, with Arrhenius-type temperature dependences. The dependence of inception on acetylene concentration is the most controversial aspect of this model. However, models of inception based on small mass PAHs have not yet been entirely validated and accepted. The Lindstedt model is felt to be the best available at this time.

Another favorable feature of the stretched flamelet approach; wherein the soot growth parameters are calculated off-line is the relative ease by which different growth models can be incorporated into the analysis, and the fact that one is not forced to oversimplify either the chemistry or the soot growth mechanism as is presently the case with transport-based approaches. The Lindstedt growth parameters used are tabulated below.

Table 3
Rate Constants, in the form $A T^b e^{-E/RT}$, for Soot Formation and
Consumption Model (units are kg, m, s, kmol, kcal, and K)

<u>Rate Constant</u>	<u>A</u>	<u>b</u>	<u>E</u>
k_i	1.35×10^6	0.0	41×10^3
k_{ii}	5.00×10^2	0.0	24×10^3
k_{iii}	1.78×10^4	0.5	39×10^3

where the rate constants are associated with inception, surface growth, oxidation and coalescence processes in the way described in Figure 15. The model in its original form solves two coupled conservation equations, one for the soot mass fraction, and one for the soot number density. The present use of these growth parameters differs from that in Ref. 33 in that they are used here with the size class representation, which provides a size distribution. Refs. 23-24 assumed a monodisperse size distribution. While the results are generally sensitive to inception rate, they are not sensitive to the mass selected for the inception species. A nominal mass of 720 a.m.u. has been assumed for the inception species. Although the model jet fuel kinetics scheme includes steps leading to benzene, only the calculated acetylene concentration is used for purposes of calculating inception rates in the Lindstedt model.

With just two Lindstedt model dependent variables, transport or balance equations for them could have been readily incorporated into the turbulent flow solver. (Examples of this can be seen in certain papers contained in Ref. 12). However, this is done on a "monodisperse" basis, that is, there would only be a single particle size at each location. Using it in conjunction with

(Soot Mass)

$$\rho S(Y_{C(S)}) = r_i M_{C(S)} + r_{ii} M_{C(S)} [C(S)]^{2/3} [N]^{1/3} - r_{iii} M_{C(S)} [C(S)]^{2/3} [N]^{1/3}$$

(Soot # Density)

$$\rho S(N) = r_{iv} - r_v [C(S)]^{1/6} [N]^{11/6},$$

where

$$r_i = k_i [C_2H_2]$$

$$r_{ii} = k_{ii} f(p) [C_2H_2]$$

$$r_{iii} = k_{iii} f'(p) [O_2]$$

$$r_{iv} = \frac{2}{C_{min}} N_A r_i$$

$$r_v = 2C_a \left(\frac{6M_{C(S)}}{\pi \rho_{C(S)}} \right)^{1/6} \left(\frac{6kT}{\rho_{C(S)}} \right)^{1/2}$$

Figure 15. The Lindstedt global soot formation model.
(Fairweather, Jones and Lindstedt, Comb. & Flame, 89, 1992)

the stretched flamelet and size class growth algorithms has the advantage that information about particle size distribution is obtained. Also, it is an open question whether monodisperse models can properly treat high pressure growth effects associated with different size particles belonging to different Knudsen Number regimes. It is felt that the size class representation used here can properly treat such effects. Ultimately, the Lindstedt model will probably be based on a small mass PAH inception scheme; stretched flamelet theory, with its ease of incorporating complex chemistry, can readily handle this, while transport-based approaches will find it all but impossible.

Sooting flamelet calculations have been carried out for the conditions given in Table 4 with strain rate as an external parameter.

Table 4

- 10.5 ATM
 - $T_A=917\text{K}$ (1190F)
 - $T_F=478\text{K}$ (400F)
 - Strain rate 2750 - 50 sec^{-1}
-

Calculated growth and oxidizing species in the model jet fuel flamelet simulation have been shown in Figure 2 for a specific value of strain rate. The temperature profile and volume fraction for this case are shown in Figure 16. The soot is seen to be incepted on the fuel side of the flame, and grows as it is transported toward the stagnation plane by convection and thermophoresis. The average soot particle size profile, reflecting the effects of surface growth and coalescence, is shown in Figure 17. Average particle sizes are much larger than those found at atmospheric pressure because of the high pressure. The calculation yields additional information that is not shown here. The particle size distribution is calculated at each point, for example, and could be provided.

The calculated soot volume fraction profiles in mixture fraction space with strain rate as an external parameter are shown in Figure 18. As seen, the soot profiles have the form of a similarity solution of the form $f_v(z, a) = h(a)g(z)$. Numerical differentiation of the profiles to give the scalar

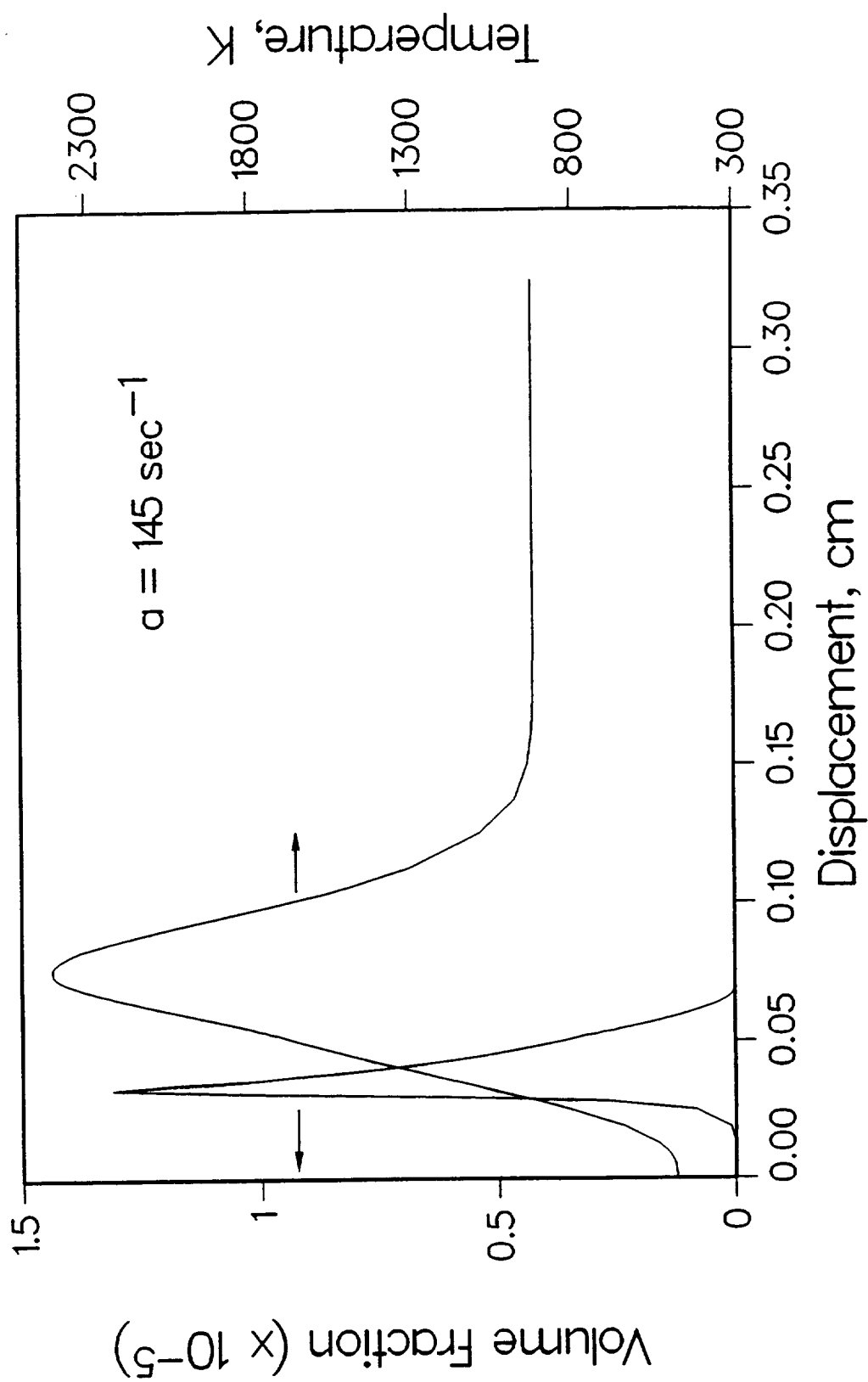


Figure 16. Soot volume fraction and temperature profiles in model jet fuel flamelet.

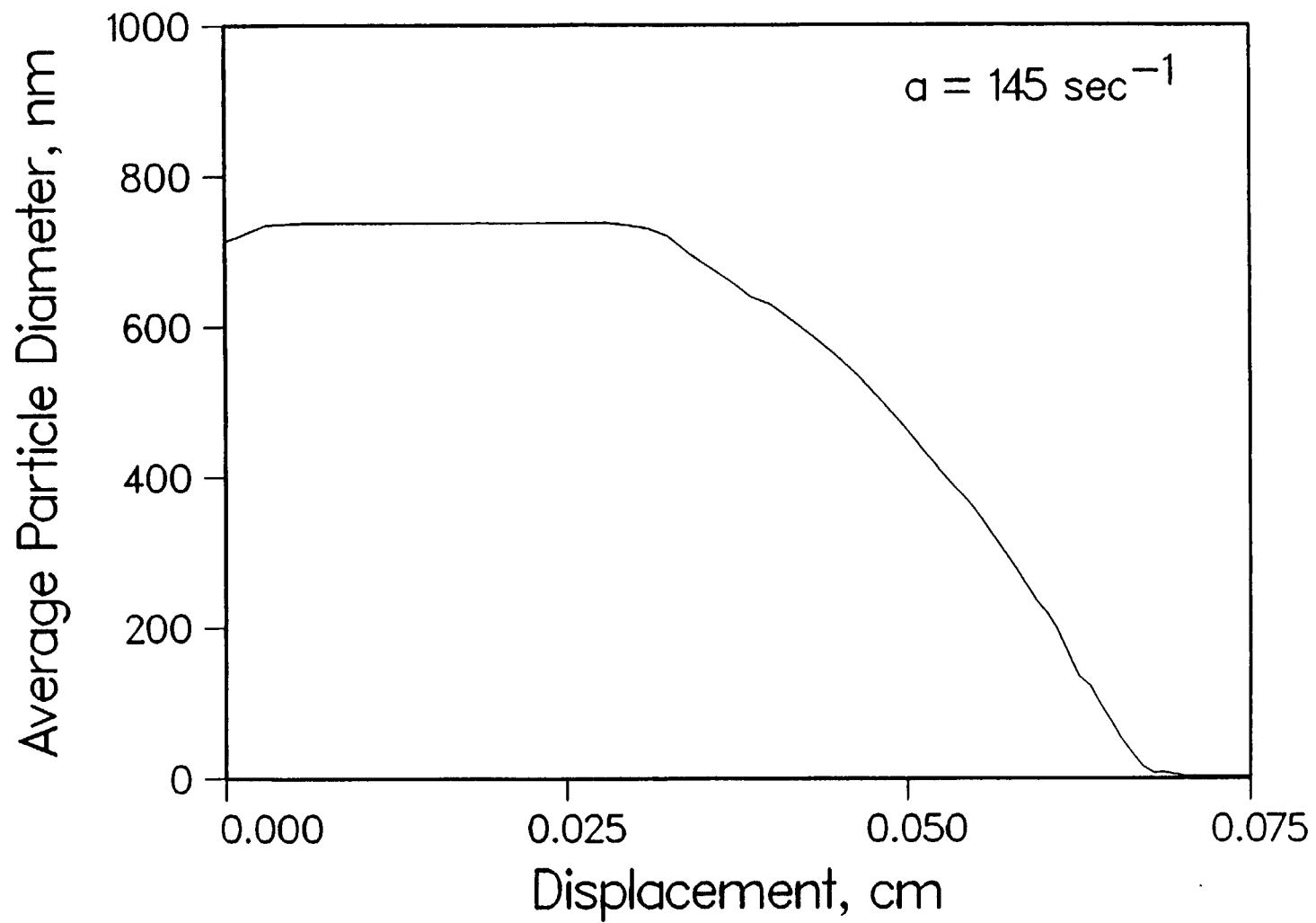


Figure 17. Average particle diameter in model jet fuel flamelet.

Fuel: 15% Trimethylbenzene, 85% Decane

Lindstedt Model; $P = 10.5$ atm

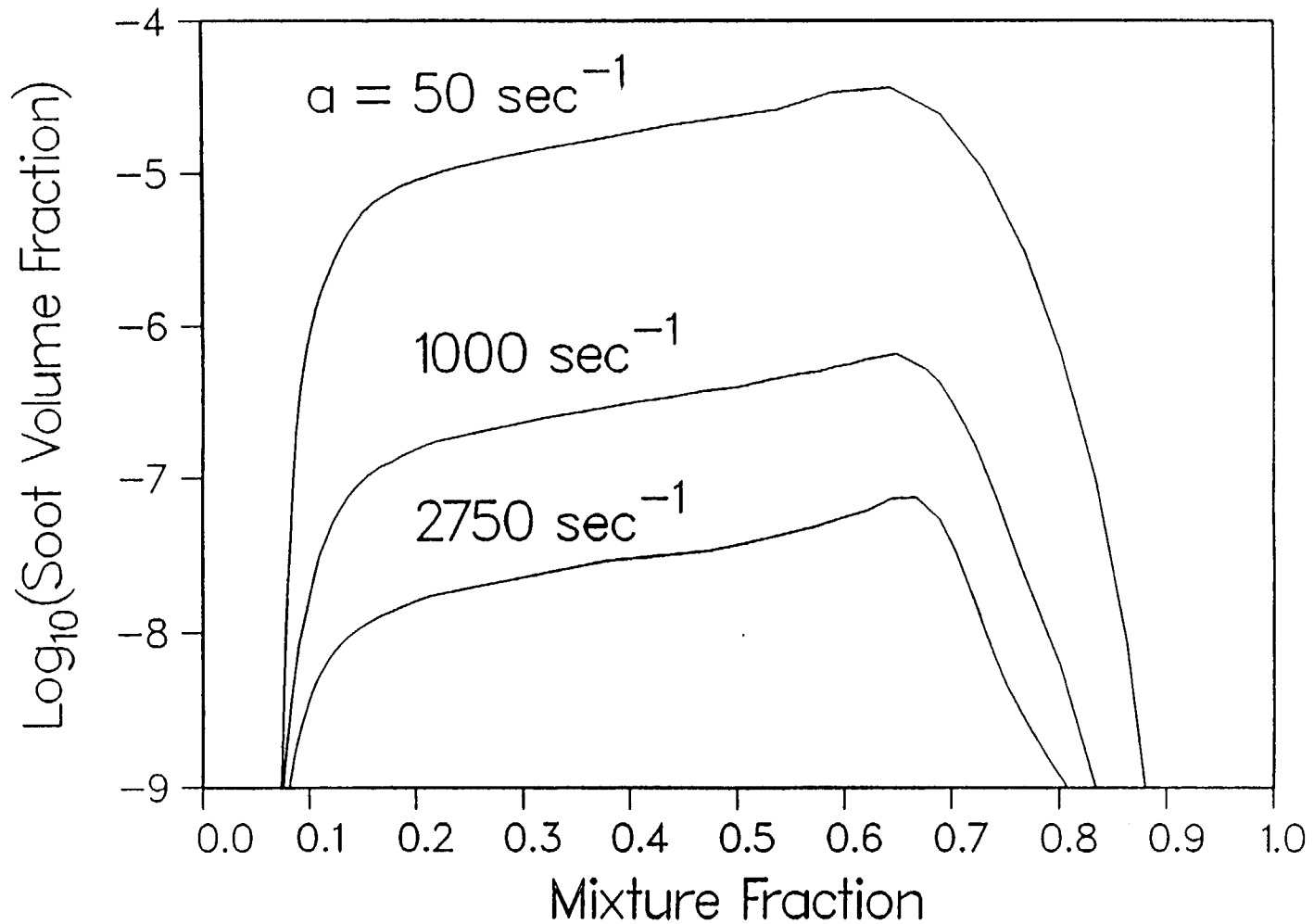


Figure 18. Strain rate dependence of soot formation in model jet fuel flamelets.

dissipation also reveals a similarity form as discussed in the preceding section on development of the joint mixture fraction/scalar dissipation pdf. The flamelet profiles contain all the information needed to formulate the joint pdf as shown in the Subtask F discussion.

While setting up the counterflow code to calculate them the first time is a cumbersome task, it is likely that this can be highly automated in the future. Work is in progress on creation of "continuation" versions of the opposed jet code, in which the range of strain rates, pressures, fuel composition and fuel/air temperatures is swept out continuously (Ref. 25). For pressure, this is likely to yield fairly simple scaling laws that can be used to correct parameters obtained at a reference pressure. Changing jet fuel kinetics mechanisms also is not a difficult task; utilities exist to convert restart files from one mechanism to another. Most of the calculational investment in the stretched flamelet approach occurs in the library setup and generation; the postprocessing calculation of soot loadings is relatively simple and efficient.

The predicted pressure dependence of the volume fraction profile for a representative strain rate is shown in Figure 19. For low to moderate pressures, soot volume fraction is about quadratic in pressure. There are many factors contributing to this dependence. As pressure increases, more complete reaction leads to higher overall temperatures in the flamelet, leading in turn to higher inception and surface growth through the Arrhenius factors of Table 3. Increased acetylene concentration also leads to increased inception and surface growth. The result is similar to that observed in pre-mixed and co-flow diffusion flames (Refs. 26-29). At much higher pressures, the expectation would be that depletion of the gaseous carbon pool would result in a pressure dependence approaching a linear relationship.

Figure 20 shows a comparison of calculations performed using the Lindstedt model with those performed using a provisional model from Ref. 22, which has inception linked to calculated benzene and phenyl concentrations. The latter model is not as well validated as the Lindstedt model, but the differences shown are probably representative of the uncertainties in soot kinetic models at this time. Use of another soot growth or jet fuel kinetics model would merely require that the curve fits

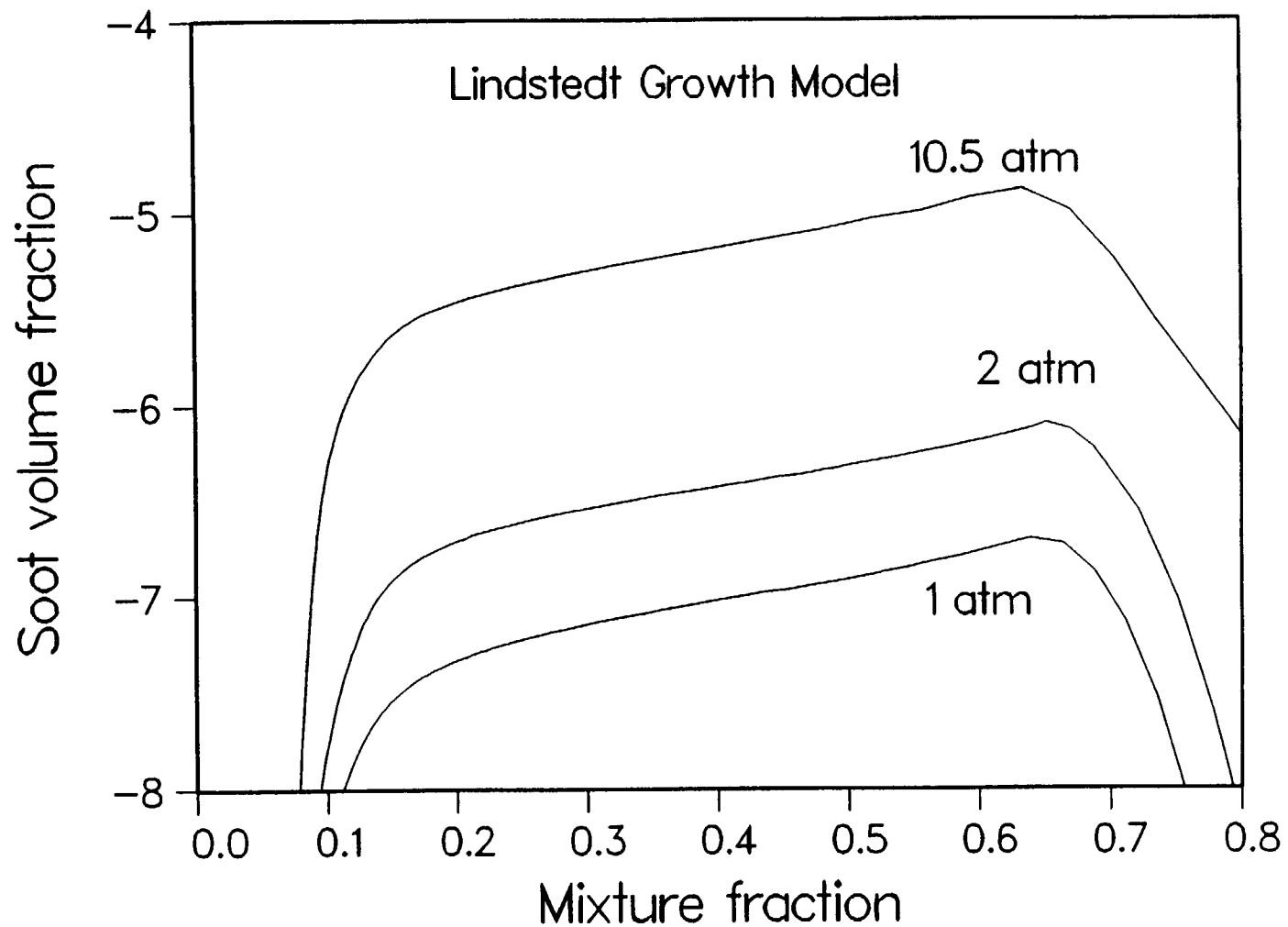


Figure 19. Pressure dependence of soot formation in model jet fuel flamelets.

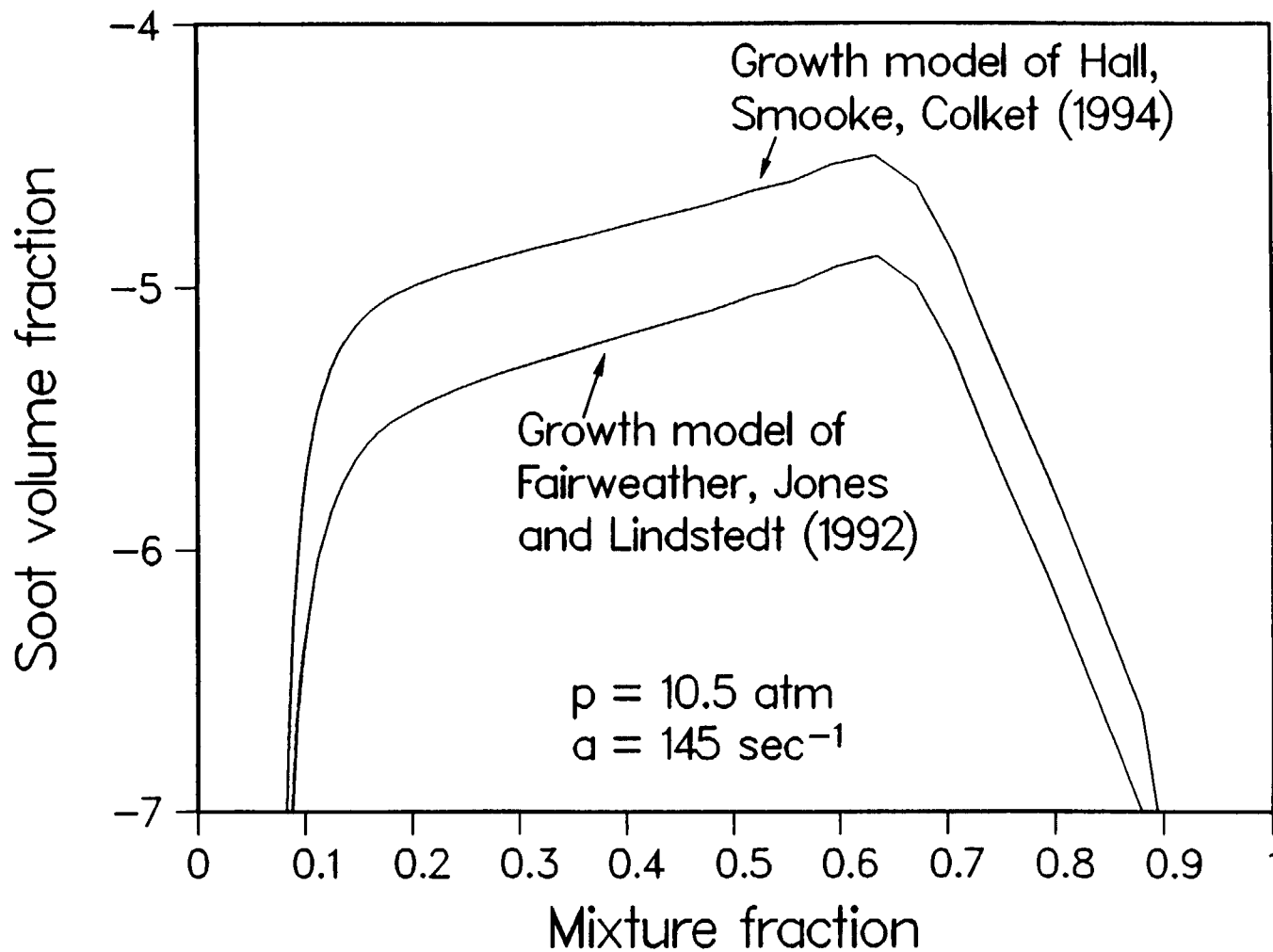


Figure 20. Comparison of soot models in jet fuel flamelets.

of the shape and similarity parameters described in the Subtask F discussion be redone, a relatively simple task.

COUPLED FLOW, SOOT GROWTH, and RADIATION PROGRAM

The sooting flamelet and radiation algorithms have been coupled to the TEACH code on a post-processing basis. The flow calculation is completed, and the converged parameters are supplied as needed input for the joint pdf and radiation calculations. This assumes that the radiation represents a small fraction of the total flow enthalpy release. Should the contrary be true in some circumstances, it would be possible in principle to perform an iterative calculation in which the flux divergence is supplied as a sink term to the energy equation for the next iteration on the flow code, and so on. While the TEACH code has been used for demonstration purposes, any other flow code whose output can be arranged to give the mean mixture fraction, its variance, and the scalar dissipation could be used.

A flow diagram showing the calculational procedure is shown in Figure 21. The contours of the axisymmetric combustor are first supplied to the program TRFN2D, which calculates the radiation grid using transfinite interpolation based on the desired number of grid points in the r and z directions. A program named READFLOW reads the output of the TEACH program; the important quantities for the soot growth and radiation calculation are the mean mixture fraction, its variance, and the scalar dissipation at each node point. The program also reads in the means of scalars like temperature, density, and the species concentrations, since this version of TEACH calculates these, but the single scalar averaging needed for these quantities can also be done in the radiation code. The output of READFLOW is then mapped onto the radiative mesh using RADMAP, which uses bilinear interpolation. RADMAP also incorporates information on wall temperatures and emissivities into its output file. The radiation grid, the output of RADMAP, and a flamelet library for single scalar pdf calculations are then input to the discrete transfer program, RADCALC. The curve-fits of the sooting flamelet library calculations (Subtask F) are incorporated into a subroutine JOINTPDF, which is linked to RADCALC. The options available in RADCALC

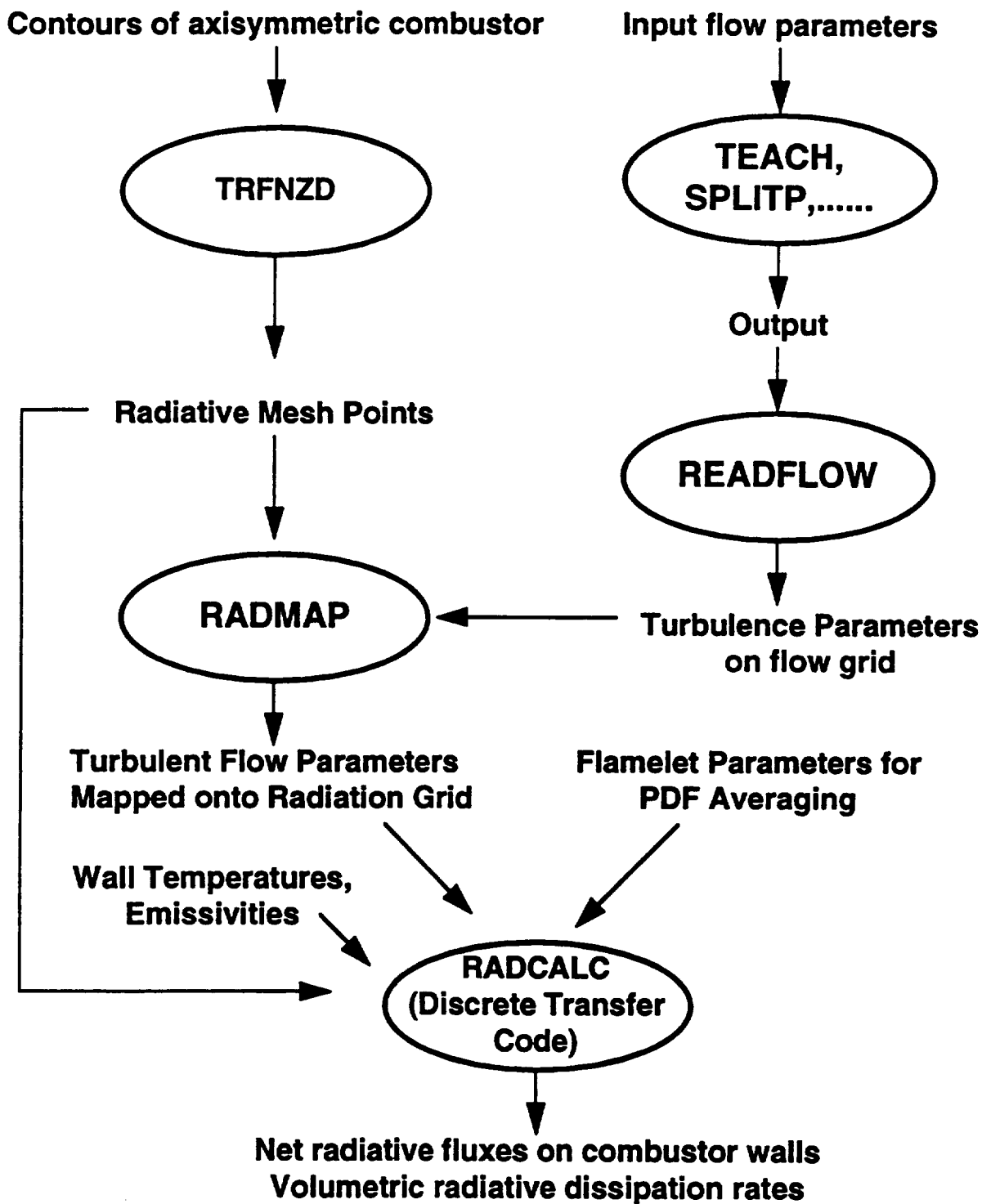


Figure 21. Radiation code flow diagram.

are a radiation calculation based on time-averaged properties, and a calculation using the turbulent radiation algorithm which has been discussed. When the time averaged property option is selected, there is also the option of doing narrowband calculations using RADCAL (Ref. 20). The input also includes the number of rays to be used in the discrete transfer analysis, in the manner described in Refs. 18-19. The output of the program consists of the net radiative fluxes on all walls, and the volumetric radiative dissipation rate. Output is in KW/M² and KW/M³, respectively. Nominally 32 rays per point per quadrant are used in the discrete transfer analysis.

Sample calculations have been carried out for the decane-fuelled, bluff-body dump combustor configuration shown previously in Figure 3. The geometry is of a type in use at Wright-Patterson Air Force Base (Ref. 30). In the base configuration, fuel is injected at the middle of a center-body face through a .96 cm diameter tube; the overall diameter of the centerbody is 14 cm, and the airstream is located from radial location 7 cm to the outer wall whose radius is 12.7 cm (5 inches). The pressure, equivalence ratio, and fuel/air stream temperatures are representative of conditions of practical interest. However, the combustor is of a type intended for diagnostic studies and is relatively slow mixing; the calculations to follow are intended only as numerical exercises, and are not meant to represent a combustor of commercial interest. Experiments in such a simple geometry would be ideal for model validation.

The average temperature distribution in the model calculation is shown in Figure 22. The relative slowness of the mixing is indicated by the fact that the average temperature level is still rising at two meters. These average temperatures were calculated using a single scalar, mixture fraction pdf, since temperature is only slowly varying with strain rate, and there is no need to use the joint pdf. Corresponding mean mixture fraction and scalar dissipation distributions are shown in Figure 23. The scalar dissipation, in units sec⁽⁻¹⁾, is seen to die away relatively rapidly with distance from the fuel injector. These quantities, together with the mixture fraction variance, are needed for the single scalar and joint pdf averaging algorithms. Application of the joint pdf results in the calculated average soot distribution shown in Figure 24. The soot peaks on the centerline

Average T;Single Scalar PDF

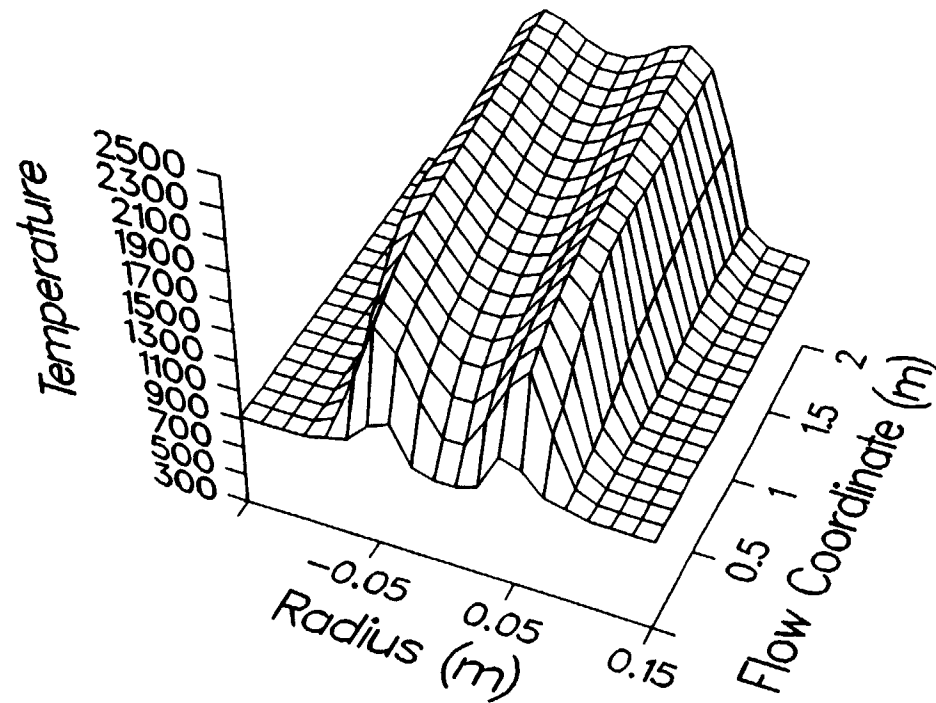
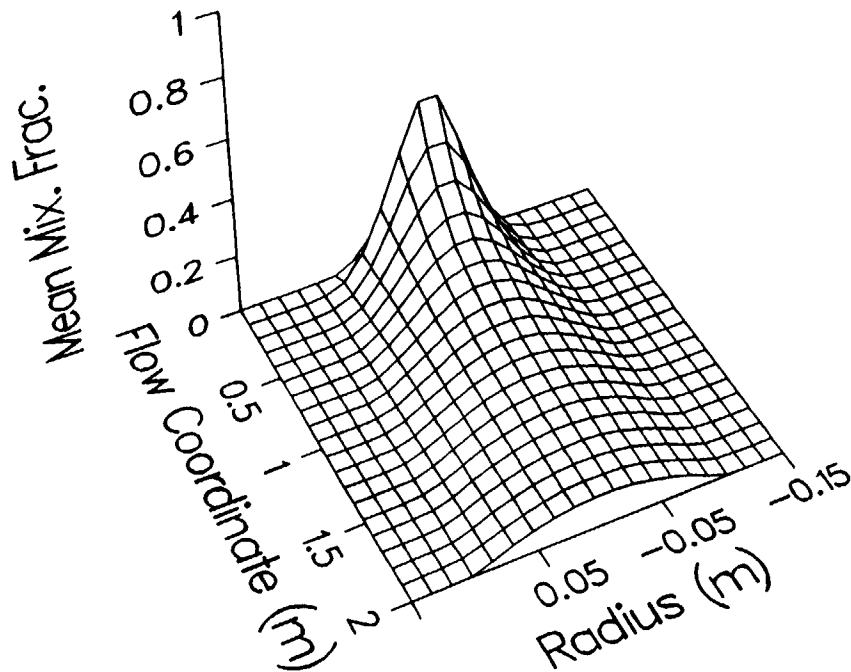
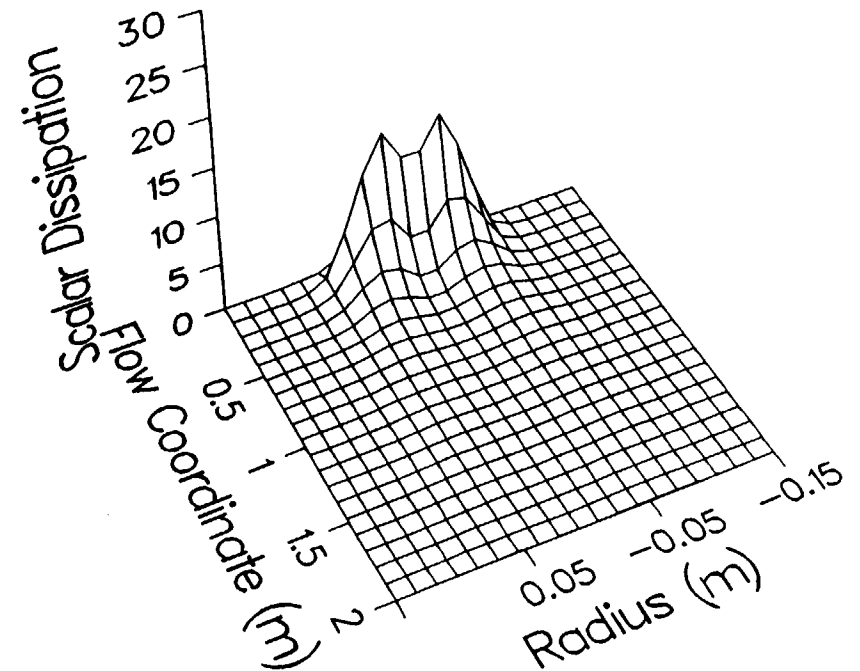


Figure 22. Temperature distribution in dump combustor simulation.

MEAN MIXTURE FRACTION



SCALAR DISSIPATION

**Figure 23. Mean mixture fraction and scalar dissipation in dump combustor simulation.**

Stretched Flamelet Theory

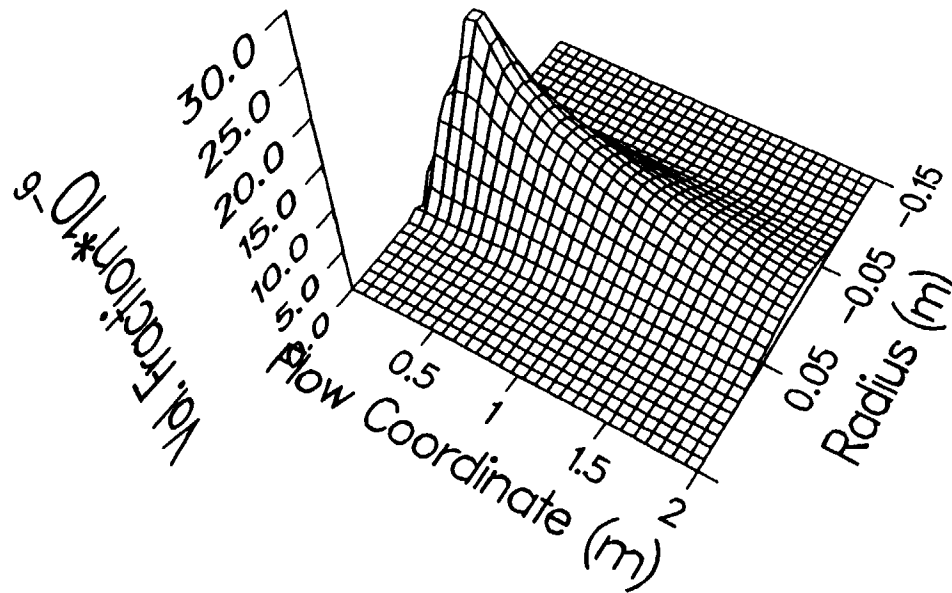


Figure 24. Soot distribution in dump combustor simulation.

near the fuel injector at values somewhat in excess of $10^{(-5)}$ and dies away over the course of the two meter length. Peak soot volume fractions in ten atmosphere, kerosene-fuelled combustors are known to be of this magnitude (Ref. 31); while much more precise theory-experiment validation is necessary before any conclusions can be drawn, this is preliminary encouragement that these first calculations of soot growth in high pressure combustors are of the right order. (Soot loadings are sometimes given in units of grams per cubic meter. The predicted peak soot volume fractions in this simulation are on the order of 40 g/m^3 . There is experimental evidence that primary zone soot concentrations at ten atmospheres are indeed about this level (Ref. 31)).

Averaging out the strain rate in the joint pdf gives the pdf in terms of mixture fraction, illustrated at the point of maximum soot in Figure 25. Whereas in an individual flamelet the volume fraction maximum occurs at a mixture fraction of about .65, near the stagnation plane, the joint pdf maximum occurs at lower mixture fractions around .4. This reflects the effects of flamelet stretching by the turbulent flow.

Net radiative fluxes on the cylindrical wall are shown in Figures 26-28. The pure soot, pure gas, and gas plus soot on a time-averaged basis are shown in Figure 26. Soot radiation is seen to dominate the gas radiation for soot levels of this magnitude. The gas radiation is dominated by the 4.3 micron band of CO_2 . The good agreement of the present radiation model with spectrally-integrated, narrowband calculations is shown in Figure 27, again on a time-averaged basis. The present wideband-based model of Equations 25, 31 and 32 is much more efficient than the narrow-band calculations, and gives agreement that is entirely satisfactory. Comparison to a prediction using the turbulent radiation algorithm shows that in this case, turbulence is predicted to result in an enhancement of somewhat less than 20% relative to calculations based on time-averaged properties (Figure 28). Because the double integration involved in the joint pdf is at present quite time-consuming, the turbulent radiation algorithm as it relates to soot is in the code in an approximate form. The temperature is allowed to fluctuate according to the single scalar pdf, using the average volume fraction calculated with the joint pdf. A priority item for future work must be to

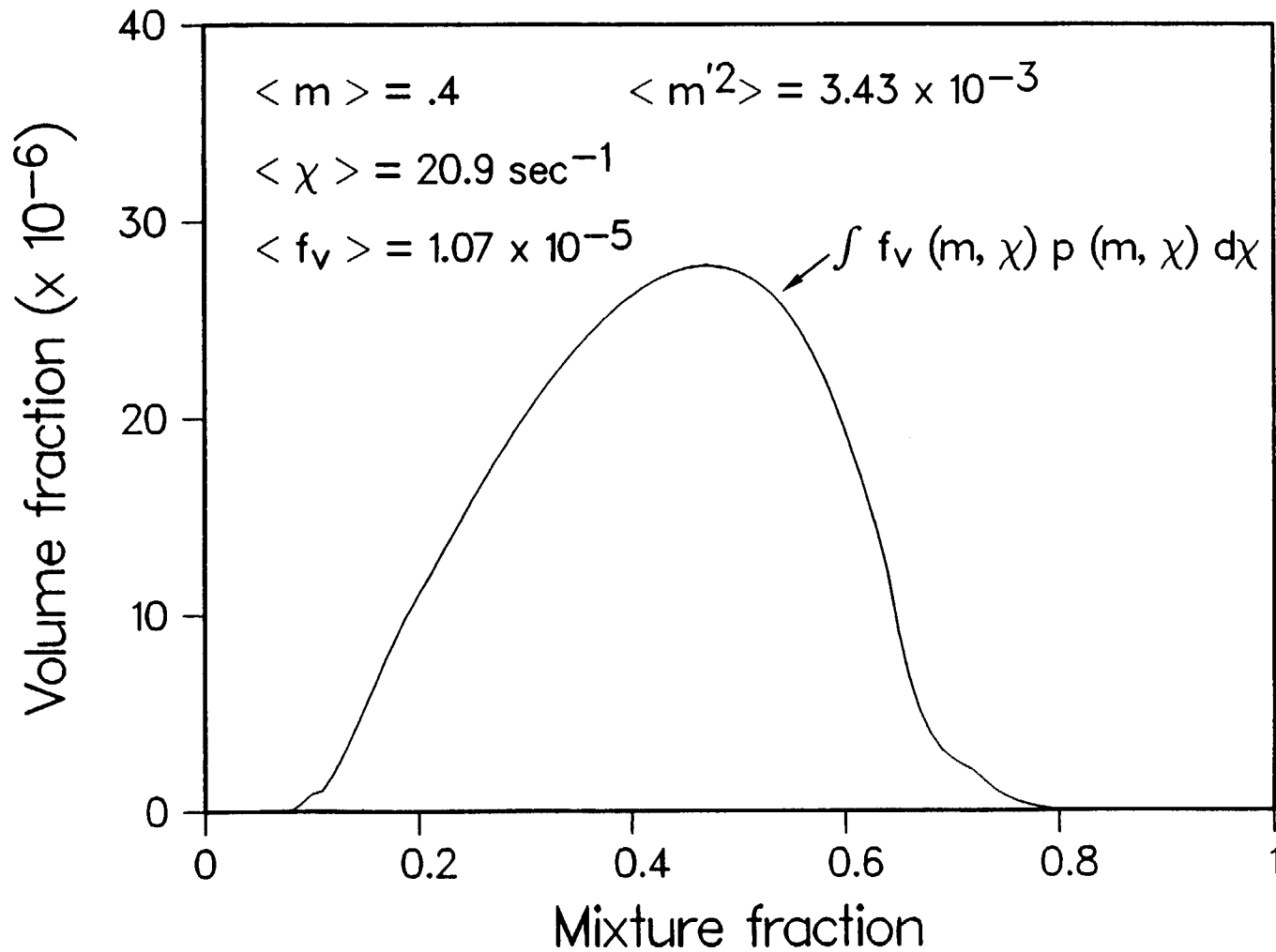


Figure 25. Joint mixture fraction/scalar dissipation PDF in model jet fuel/dump combustor simulation.

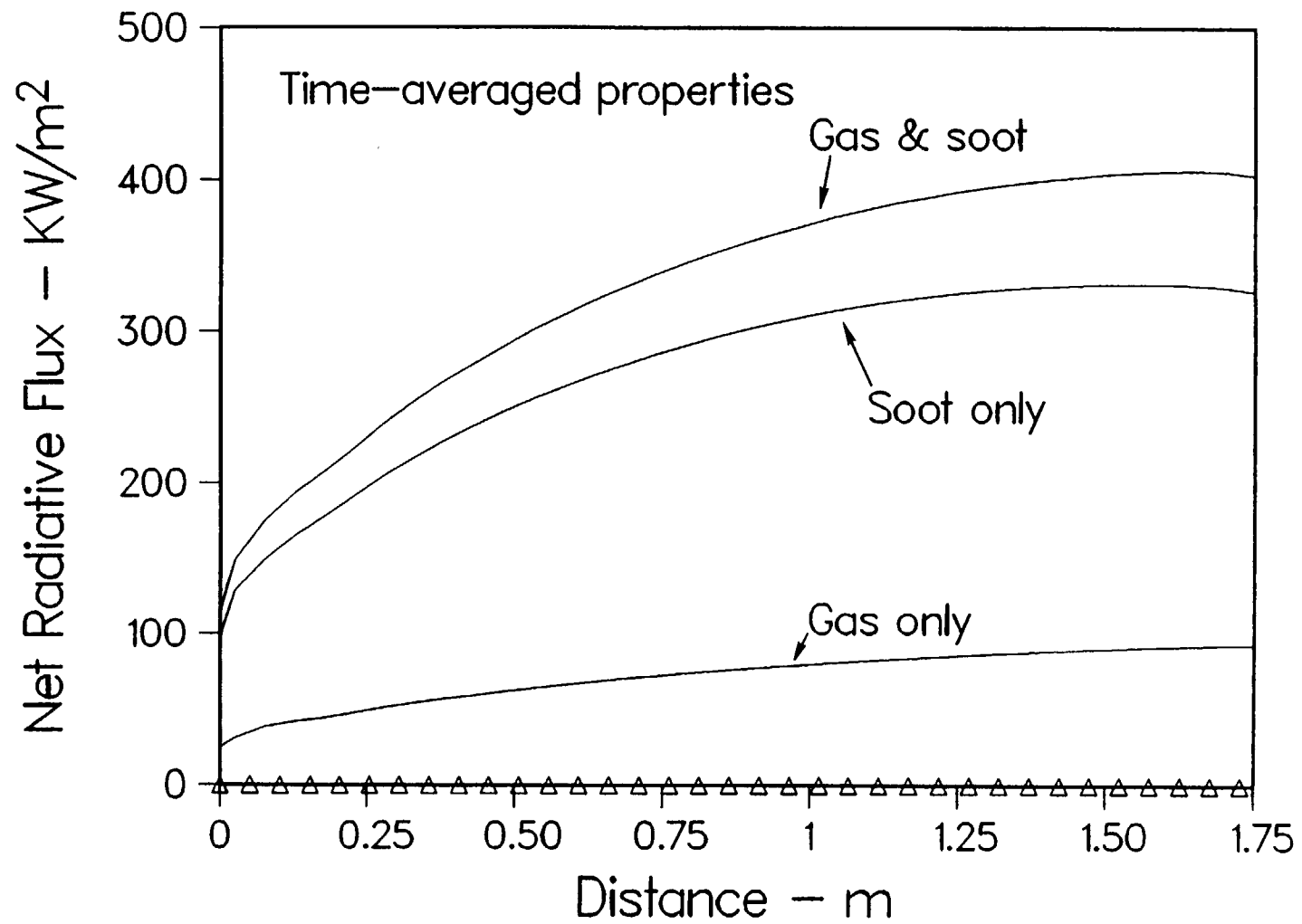


Figure 26. Soot and gas radiation fluxes on dump combustor wall.

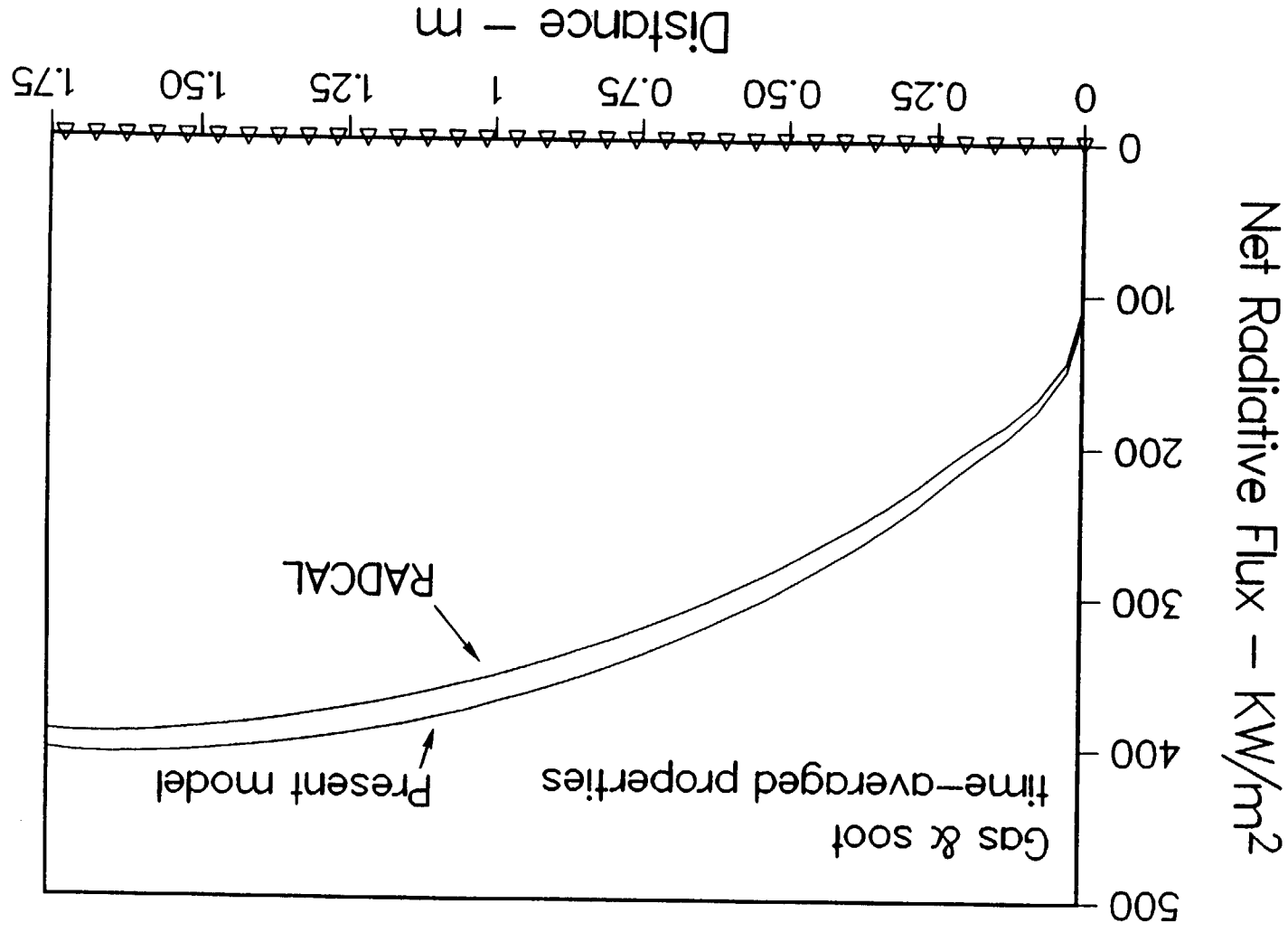


Figure 27. Wideband and narrowband radiation models compared.

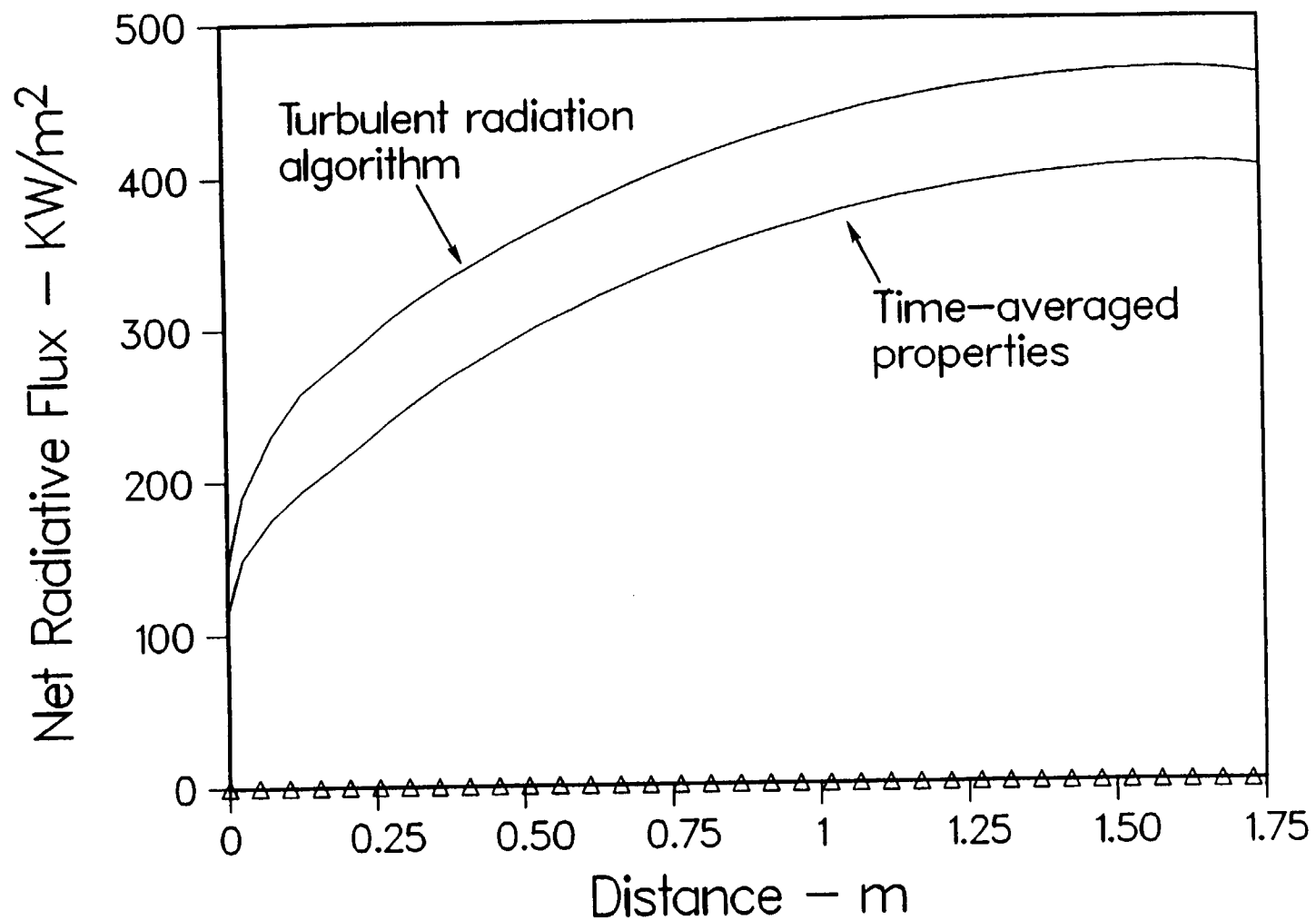


Figure 28. Turbulence enhancement of radiation on dump combustor walls.

find a more efficient double integration technique.

The radiative dissipation profile on a time-averaged basis is shown in Figure 29, corresponding to the contributions of both gas and soot. The dissipation rate (net radiative emission rate) tends to follow the temperature distribution to an exaggerated extent because of the sensitivity of the Planck function to temperature (Compare Figure 22). Because of the time-consuming nature of the joint pdf calculation, radiative dissipation is presently calculated only on a time-averaged property basis; only the fluxes on the walls are calculated using the turbulent radiation algorithm, and not the internal fields needed for the dissipation calculation. The radiative source term could be supplied as an energy sink term to the flow code energy equation for an iterative calculation to see whether radiation significantly depresses average temperatures. The dissipation rate is the local emission rate minus the rate of absorption of radiation from other parts of the combustor; note in Figure 29 a region of cold soot on the centerline near the fuel injector in which there is net absorption of radiation.

Extensive parametric variations have not yet been carried out with this model. Changing the fuel and air flow rates by the same factors is found to result in a mixture fraction/mixture fraction variance profile that is sensibly unchanged in spatial coordinates. The peak scalar dissipation does scale with velocity in the manner expected, but its influence is confined to a relatively small region near the fuel nozzle. The result is a soot profile that is relatively insensitive to the velocities of the streams (keeping equivalence ratio constant). The radiative wall fluxes are similarly insensitive, implying that the fraction of the total enthalpy converted to radiation is inversely proportional to velocity at constant equivalence ratio. The predicted pressure dependence of the soot volume fraction would approximate that of the flamelets; that is, it would be about quadratic for pressures in the vicinity of ten atmospheres or below, and would be expected to make a transition from quadratic to linear at much higher pressures.

A sample, provisional, application of this soot formation theory to the RBQQ sector rig is shown in Figure 30. A three-dimensional CFD flowfield simulation was obtained courtesy of CFD

Stretched Flamelet Theory

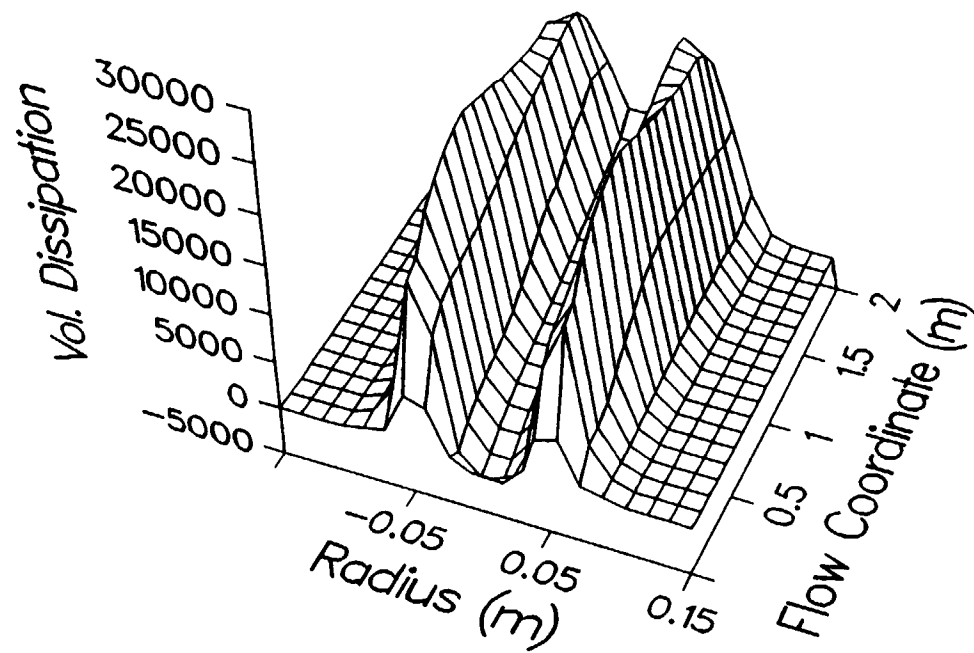


Figure 29. Radiative dissipation in dump combustor simulation.

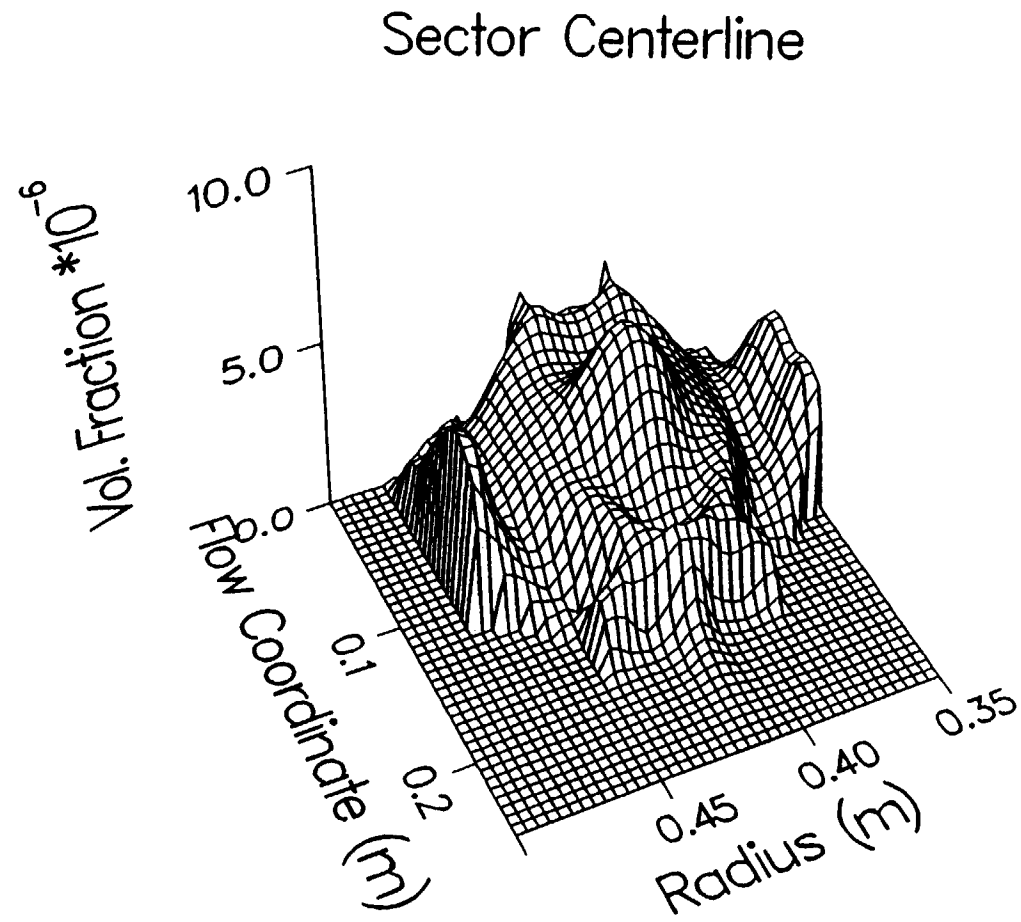


Figure 30. Soot distribution in RQL combustor simulation.

Research, Inc. From the provided profiles of mean mixture fraction, its variance, and the scalar dissipation, values were extracted along the center of the sector rig, and soot loadings calculated using the joint PDF algorithm. As seen, peak soot volume fractions in the rich zone approach 10^{-5} . The soot is seen to be very effectively oxidized in the quench zone.

CONCLUSIONS AND RECOMMENDATIONS FOR FUTURE WORK

These investigations have lead to a number of noteworthy technical achievements. Among these is the first calculation of soot formation in jet fuel based on a complex chemical mechanism. The associated soot growth calculations are the first to incorporate continuum effects in the particle kinetics scheme in order to treat high pressure growth. Further, this work marks the first inclusion of efficient turbulence-radiation interactions algorithms into a radiation code. The inclusion of non-linear effects in the k- ϵ flow code and the formulation of a joint mixture fraction/scalar dissipation pdf for turbulent soot formation from the stretched flamelet calculations are also significant technical aspects. In the model jet fuel, predicted soot levels appear to be of the right order when compared to primary zone data at elevated pressure. However, these data are limited; before this analysis can be applied with confidence as a design tool, future work directed towards model validation and enhancement should be undertaken.

Model validation studies would involve comparisons with turbulent jet data, starting with simpler fuels like ethylene and propane. In terms of other basic experimental data, there is a strong need for high pressure, sooting opposed jet experiments, starting with ethylene, and progressing to more complex fuels. Well-diagnosed model combustor experiments providing soot volume fractions and radiative fluxes also would be invaluable.

Certain model enhancements could be undertaken. Among these would be sensitivity analyses and simplification of the jet fuel kinetics mechanism. Simplified correlations and scaling relationships linking soot levels to pressure, strain rate, and fuel/air temperatures can be developed to obviate the need to generate new flamelet libraries. As new information on soot inception and sur-

face growth becomes available, these would be evaluate for impact on jet fuel soot formation. The basic stretched flamelet theory could be enhanced by consideration of partial premixing, flamelet-flamelet interactions, and non-adiabatic loss.

While the TEACH code was employed in these demonstration calculations, any flow code that can be configured to provide the required joint pdf parameters could be employed. Thus, for example, extensions to unstructured grid codes such as CORSAIR would not be a complicated matter. The discrete transfer radiation algorithm used here has considerable geometric flexibility.

NOMENCLATURE

a	beta density parameter; strain rate in opposed jet flame
A	band absorptance
A'	band absorptance derivative
b	beta density parameter
c_1, c_2	Planck function constants
c_s	factor in soot absorption coefficient
D	soot diameter
E_1	exponential integral
f_v	soot volume fraction
H	height above burner surface
I	radiative intensity
I_b	Planck function
k	absorption coefficient
p	probability density for mixture fraction
R_0	fuel tube radius
s	optical pathlength
T	gas temperature
z	fuel mixture fraction
z'	fluctuation in mixture fraction

Greek symbols

α	integrated band intensity
χ	scalar dissipation
Δ	Length of locally homogeneous portion of inhomogeneous path
ϵ	emissivity
γ	parameter in beta density
γ_E	Euler-Mascheroni constant
Γ	Gamma function
λ	thermal radiation wavelength
η_i	probability density parameter
$\Delta\omega$	bandwidth
ξ	band intensity path integral
ρ	radiating gas density
ω	frequency
$\omega^{(0)}$	band center frequency

Subscripts

i	i-th molecular resonance
w	wall value

REFERENCES

1. Southern Petroleum Laboratories Internal Report, 1991; Pratt & Whitney Aircraft (ASTM D1319 and D2789).
2. C.G. Speziale, On Non-Linear $k-\ell$ and $k-\epsilon$ Models of Turbulence, *J. Fluid Mech.* **178**, 459-475 (1987).
3. C.G. Speziale, Some Interesting Properties of Two-Dimensional Turbulence, *Phys. Fluids* **24**, 1425-1427 (1981).
4. A. Vranos, A Generalized Conditional Scalar Dissipation-Mixture Fraction Joint PDF for Flamelet Modeling of Non-Premixed Flames, *Combust. Sci. and Tech.*, **84**, 323-334 (1992).
5. V.P. Kabashnikov and G.I. Kmit, Influence of Turbulent Fluctuations on Thermal Radiation, *J. Appl. Spectr.* **31**, 963-967 (1979).
6. M.E. Kounalakis, J.P. Gore, and G.M. Faeth, Turbulence/Radiation Interactions in Non-premixed Hydrogen/Air Flames, *Twenty-second Symposium (International) on Combustion/The Combustion Institute*, 1281-1290 (1988).
7. J.P. Gore and G.M. Faeth, Structure and Spectral Radiation Properties of Turbulent Ethylene/Air Diffusion Flames, *Twenty-first Symposium (International) on Combustion/The Combustion Institute*, 1521-1531 (1986).
8. R.J. Hall and A. Vranos, Efficient Calculations of Gas Radiation from Turbulent Flames, *Int'l J. Heat and Mass Trans.*, **37**, 2745-2750 (1994).
9. R.J. Hall and A. Vranos, Incorporation of an Efficient Turbulent Radiation Algorithm into a Discrete Transfer Program, 2nd Eurotherm Proceedings, 491-502 (1994).
10. W. Krebs, R. Koch, A.J. Bauer, R. Kneer and S. Wittig, Effect of Turbulence on Radiative Heat Transfer Inside a Model Combustor, *2nd Eurotherm Proceedings*, 349-362 (1994).
11. D.K. Edwards and A. Balakrishnan, Thermal Radiation by Combustion Gases, *Intl. J. Heat Mass Transfer* **16**, 25-32 (1973).
12. Proceedings of 1st and 2nd Eurotherm Conferneces on Heat Transfer in Radiating and Combusting Systems, Cascais, Portugal, Oct. 8-10, 1990; Turin, Italy, Oct. 5-7, 1994.
13. N. Lallemand and R. Weber, Evaluation of Seven Approximate Emissivity Models for CFD Modelling of Non-Luminous Flames, *2nd Eurotherm Proceedings*, 109-124 (1994).
14. D.K. Edwards and S.J. Morizumi, Scaling of Vibration-Rotation Band Parameters for Nonhomogeneous Gas Radiation, *J. Quant. Spectrosc. Radiat. Transfer* **10**, 175-188 (1970).
15. A. Vranos, et. al., Nitric Oxide Formation and Differential Diffusion in a Turbulent Methane-Hydrogen Diffusion Flame, *Twenty-fourth Symposium (International) on Combustion/The Com-*

bustion Institute, 377-384 (1992).

16. J. Janicka and W. Kollman, A Two-Variable Formalism for the Treatment of Chemical Reactions in Turbulent H₂-Air Diffusion Flames, *Seventeenth Symposium (International) on Combustion/ The Combustion Institute*, 421-429 (1978).
17. M.D. Smooke, I.K. Puri, and K. Seshadri, A Comparison Between Numerical Calculations and Experimental Measurements of the Structure of a Counterflow Diffusion Flame Burning Diluted Methane in Diluted Air, *Twenty-first Symposium (International) on Combustion, The Combustion Institute*, 1783-1792 (1986).
18. F.C. Lockwood and N.G. Shah, A New Radiation Solution Method for Incorporation in General Combustion Prediction Procedures, *Eighteenth Symposium (International) on Combustion, The Combustion Institute*, 1405- 1412 (1981).
19. N.G. Shah, New Method of Computation of Radiation Heat Transfer in Combustion Chambers, PhD Thesis, University of London, 1979.
20. W.L. Grosshandler, *RADCAL: A Narrow-Band Model for Radiation Calculations in a Combustion Environment*, NIST Technical Note 1402 (1993).
21. R.J. Hall, Radiative Dissipation in Planar Gas-Soot Mixtures, *JQSRT*, **51**, 635-644 (1994).
22. R.J. Hall, M.D. Smooke, and M.B. Colket, Predictions of Soot Dynamics in Opposed Jet Diffusion Flames, accepted for publication in *Combustion Science and Technology Book Series* (1995).
23. M. Fairweather, W.P. Jones, and R.P. Lindstedt, Predictions of Radiative Transfer from a Turbulent Reacting Jet in a Cross-Wind, *Combustion and Flame*, **89**, 45-63 (1992).
24. Y.R. Sivathanu and J.P. Gore, Radiation and Soot Kinetics Interaction in Acetylene/Air Diffusion Flames, *Central/Eastern States Combustion Institute Joint Meeting*, New Orleans, March 15-17 (1993); *Combustion and Flame*, **97**, 161-172 (1994).
25. V. Giovangigli and M.D. Smooke, Adaptive Continuation Algorithms with Application to Combustion Problems, *App. Num. Math.*, **5**, (1989).
26. W.L. Flower and C.T. Bowman, *Twentieth Symposium (International) on Combustion*, The Combustion Institute, Pittsburgh, 1035-1044 (1984).
27. W.L. Flower and C.T. Bowman, *Twenty-First Symposium (International) on Combustion*, The Combustion Institute, Pittsburgh, 1115-1124 (1986).
28. A. Kazakov, H. Wang, and M. Frenklach, Detailed Modeling of Soot Formation in Laminar Premixed Ethylene Flames at a Pressure of 10 Bar, in press, *Combustion and Flame* (1994).
29. W. Lee, T.F. Richardson and R.J. Santoro, The Effects of Operating Pressure on Soot Formation in Laminar Diffusion Flames, *Central/Eastern States Combustion Institute Joint Meeting*,

New Orleans, March 15-17 (1993).

30. W.M. Roquemore and R.L. Britton, Investigation of the Dynamic Behavior of a Bluff Body Diffusion Flame Using Flame Emission, *AIAA-82-0178* (1982).
31. Y.S.H. Najjar and E.M. Goodger, Radiation and Smoke From the Gas Turbine Combustor Using Heavy Fuels, *Trans. ASME*, **105**, 82-88 (1983).

APPENDIX A

Reaction Mechanism Rate Coefficients in the Form $k_f = AT^\beta \exp(-E_0/RT)$.

Units are moles, cubic centimeters, seconds, Kelvins, and calories/mole.

	REACTION	A	β	E
1.	H+O2=O+OH	5.10E16	-0.820	16510.
2.	H2+O=H+OH	1.80E10	1.0	8830.
3.	H2+OH=H2O+H	1.20E09	1.3	3630.
4.	OH+OH=H2O+O	6.0E08	1.3	0.
5.	H+OH+M=H2O+M (M=AR) H2O/20./	7.50E23	-2.6	0.
6.	O2+M=O+O+M	1.90E11	0.5	95560.
7.	H+H+M=H2+M (M=AR) H2O/0.0/H2/0.0/CO2/0.0/	1.0E18	-1.0	0.
8.	H+H+H2=H2+H2	9.20E16	-0.6	0.
9.	H+H+H2O=H2+H2O	6.00E19	-1.250	0.
10.	H+H+CO2=H2+CO2	5.49E20	-2.0	0.
11.	H2+O2=OH+OH	1.70E13	0.0	47780.
12.	H+O2+M=HO2+M (M=AR) H2O/21./CO2/5./H2/3.3/CO/2./O2/0./N2/0./	2.10E18	-1.0	0.
13.	H+O2+O2=HO2+O2	6.70E19	-1.420	0.
14.	H+O2+N2=HO2+N2	6.70E19	-1.420	0.
15.	HO2+H=H2+O2	2.50E13	0.	700.
16.	HO2+H=OH+OH	2.50E14	0.	1900.
17.	HO2+O=OH+O2	4.80E13	0.	1000.
18.	HO2+OH=H2O+O2	5.00E13	0.	1000.
19.	HO2+HO2=H2O2+O2	2.00E12	0.	0.
20.	H2O2+M=OH+OH+M	1.20E17	0.	45500.
21.	H2O2+H=HO2+H2	1.70E12	0.0	3750.
22.	H2O2+OH=H2O+HO2	1.00E13	0.0	1800.
23.	CO+O+M=CO2+M	3.20E13	0.0	-4200.
24.	CO+O2=CO2+O	2.50E12	0.	47700.
25.	CO+OH=CO2+H	1.50E07	1.3	-760.
26.	CO+HO2=CO2+OH	5.80E13	0.	22930.
27.	CH4+M=CH3+H+M (M=AR) H2O/5./	1.00E17	0.	88000.
28.	CH4+H=CH3+H2	2.20E04	3.0	8750.
29.	CH4+O=CH3+OH	1.20E07	2.080	7630.
30.	CH4+OH=CH3+H2O	3.50E03	3.080	2000.
31.	CH4+CH2=CH3+CH3	1.30E13	0.	9500.
32.	CH3+M=CH2+H+M	1.90E16	0.	91600.
33.	CH3+CH3=C2H6	1.60E13	0.0	-306.
34.	CH3+CH3=C2H4+H2	2.10E14	0.0	19200.
35.	CH3+CH2=C2H4+H	3.00E13	0.0	0.

36.	$\text{CH}_3 + \text{H} = \text{CH}_2 + \text{H}_2$	9.00E13	0.	15100.
37.	$\text{CH}_3 + \text{O} = \text{CH}_2\text{O} + \text{H}$	6.80E13	0.	0.
38.	$\text{CH}_3 + \text{O} = \text{CH}_2 + \text{OH}$	5.00E13	0.	12000.
39.	$\text{CH}_3 + \text{OH} = \text{CH}_2 + \text{H}_2\text{O}$	1.50E13	0.	5000.
40.	$\text{CH}_3 + \text{OH} = \text{CH}_2\text{O} + \text{H}_2$	1.00E12	0.	0.
41.	$\text{CH}_3 + \text{O}_2 = \text{CH}_2\text{O} + \text{OH}$	5.20E13	0.	34570.
42.	$\text{CH}_3 + \text{O}_2 = \text{CH}_3\text{O} + \text{O}$	7.00E12	0.	25650.
43.	$\text{CH}_3\text{O} + \text{M} = \text{CH}_2\text{O} + \text{H} + \text{M}$	1.00E14	0.	25000.
44.	$\text{CH}_3\text{O} + \text{H} = \text{CH}_2\text{O} + \text{H}_2$	2.00E13	0.0	0.
45.	$\text{CH}_3\text{O} + \text{O} = \text{CH}_2\text{O} + \text{OH}$	1.00E13	0.	0.
46.	$\text{CH}_3\text{O} + \text{OH} = \text{CH}_2\text{O} + \text{H}_2\text{O}$	1.00E13	0.	0.
47.	$\text{CH}_3\text{O} + \text{O}_2 = \text{CH}_2\text{O} + \text{HO}_2$	6.30E10	0.	2600.
48.	$\text{CH}_2\text{O} + \text{M} = \text{HCO} + \text{H} + \text{M}$	3.31E16	0.0	81000.
49.	$\text{CH}_2\text{O} + \text{H} = \text{HCO} + \text{H}_2$	2.20E08	1.770	10500.
50.	$\text{CH}_2\text{O} + \text{O} = \text{HCO} + \text{OH}$	1.80E13	0.0	3080.
51.	$\text{CH}_2\text{O} + \text{OH} = \text{HCO} + \text{H}_2\text{O}$	3.40E09	1.180	-447.
52.	$\text{HCO} + \text{M} = \text{CO} + \text{H} + \text{M}$	1.60E14	0.	14700.
53.	$\text{HCO} + \text{H} = \text{CO} + \text{H}_2$	4.00E13	0.0	0.0
54.	$\text{HCO} + \text{O} = \text{CO} + \text{OH}$	3.00E13	0.0	0.0
55.	$\text{HCO} + \text{O} = \text{CO}_2 + \text{H}$	3.00E13	0.0	0.0
56.	$\text{HCO} + \text{OH} = \text{CO} + \text{H}_2\text{O}$	5.00E12	0.0	0.0
57.	$\text{HCO} + \text{O}_2 = \text{CO} + \text{HO}_2$	3.30E13	-0.4	0.0
58.	$\text{CH}_2 + \text{H} = \text{CH} + \text{H}_2$	7.30E17	-1.560	0.
59.	$\text{CH}_2 + \text{O} = \text{CO} + \text{H} + \text{H}$	3.00E13	0.0	0.
60.	$\text{CH}_2 + \text{O} = \text{CO} + \text{H}_2$	5.00E13	0.0	0.
61.	$\text{CH}_2 + \text{O} = \text{CH} + \text{OH}$	5.00E13	0.0	12000.
62.	$\text{CH}_2 + \text{OH} = \text{CH}_2\text{O} + \text{H}$	3.00E13	0.0	0.
63.	$\text{CH}_2 + \text{OH} = \text{CH} + \text{H}_2\text{O}$	4.50E13	0.0	3000.
64.	$\text{CH}_2 + \text{O}_2 = \text{CO}_2 + \text{H} + \text{H}$	1.60E12	0.0	1000.
65.	$\text{CH}_2 + \text{O}_2 = \text{CO}_2 + \text{H}_2$	6.90E11	0.0	500.
66.	$\text{CH}_2 + \text{O}_2 = \text{CO} + \text{H}_2\text{O}$	1.90E10	0.0	-1000.
67.	$\text{CH}_2 + \text{O}_2 = \text{CO} + \text{OH} + \text{H}$	8.60E10	0.0	-500.
68.	$\text{CH}_2 + \text{O}_2 = \text{HCO} + \text{OH}$	4.30E10	0.0	-500.
69.	$\text{CH}_2 + \text{O}_2 = \text{CH}_2\text{O} + \text{O}$	2.00E13	0.0	9000.
70.	$\text{CH}_2 + \text{CO}_2 = \text{CO} + \text{CH}_2\text{O}$	1.10E11	0.0	1000.
71.	$\text{CH} + \text{O} = \text{CO} + \text{H}$	5.70E13	0.0	0.
72.	$\text{CH} + \text{OH} = \text{HCO} + \text{H}$	3.00E13	0.0	0.
73.	$\text{CH} + \text{O}_2 = \text{HCO} + \text{O}$	3.30E13	0.0	0.
74.	$\text{CH} + \text{CO}_2 = \text{HCO} + \text{CO}$	3.40E12	0.0	690.
75.	$\text{C}_2\text{H}_6 + \text{H} = \text{C}_2\text{H}_4 + \text{H} + \text{H}_2$	5.40E02	3.5	5200.
76.	$\text{C}_2\text{H}_6 + \text{OH} = \text{C}_2\text{H}_4 + \text{H} + \text{H}_2\text{O}$	8.70E09	1.050	1810.
77.	$\text{C}_2\text{H}_6 + \text{CH}_3 = \text{C}_2\text{H}_4 + \text{H} + \text{CH}_4$	5.50E-01	4.0	8280.
78.	$\text{C}_2\text{H}_4 + \text{M} = \text{C}_2\text{H}_2 + \text{H}_2 + \text{M}$	2.60E17	0.0	79350.
79.	$\text{C}_2\text{H}_4 + \text{M} = \text{C}_2\text{H}_3 + \text{H} + \text{M}$	2.60E17	0.0	96600.
80.	$\text{C}_2\text{H}_4 + \text{H} = \text{C}_2\text{H}_3 + \text{H}_2$	1.10E14	0.0	8500.
81.	$\text{C}_2\text{H}_4 + \text{OH} = \text{C}_2\text{H}_3 + \text{H}_2\text{O}$	4.80E12	0.0	1230.
82.	$\text{C}_2\text{H}_4 + \text{OH} = \text{CH}_2\text{O} + \text{CH}_3$	2.00E12	0.0	960.

83.	$\text{C}_2\text{H}_3 + \text{M} = \text{C}_2\text{H}_2 + \text{H} + \text{M}$	8.00E14	0.0	31500.
84.	$\text{C}_2\text{H}_3 + \text{H} = \text{C}_2\text{H}_2 + \text{H}_2$	4.00E13	0.0	0.
85.	$\text{C}_2\text{H}_3 + \text{O}_2 = \text{HCO} + \text{CH}_2\text{O}$	4.00E12	0.0	-250.
86.	$\text{C}_2\text{H}_2 + \text{M} = \text{C}_2\text{H} + \text{H} + \text{M}$	4.20E16	0.0	107000.
87.	$\text{C}_2\text{H} + \text{H}_2 = \text{C}_2\text{H}_2 + \text{H}$	4.10E05	2.390	860.
88.	$\text{C}_2\text{H}_2 + \text{O} = \text{CH}_2 + \text{CO}$	2.20E10	1.0	2580.
89.	$\text{C}_2\text{H}_2 + \text{OH} = \text{CH}_2\text{CO} + \text{H}$	3.20E11	0.0	200.
90.	$\text{C}_2\text{H}_2 + \text{OH} = \text{C}_2\text{H} + \text{H}_2\text{O}$	6.00E12	0.0	7000.
91.	$\text{CH}_2\text{CO} + \text{M} = \text{CH}_2 + \text{CO} + \text{M}$	3.60E15	0.0	59300.
92.	$\text{CH}_2\text{CO} + \text{H} = \text{CH}_3 + \text{CO}$	1.10E13	0.0	3430.
93.	$\text{CH}_2\text{CO} + \text{O} = \text{CH}_2\text{O} + \text{CO}$	2.0E13	0.0	0.
94.	$\text{CH}_2\text{CO} + \text{OH} = \text{CH}_2\text{O} + \text{HCO}$	2.80E13	0.0	0.0
95.	$\text{C}_2\text{H} + \text{O} = \text{CH} + \text{CO}$	5.00E13	0.0	0.
96.	$\text{C}_2\text{H} + \text{O}_2 = \text{CO} + \text{HCO}$	2.40E12	0.0	0.
97.	$\text{C}_{10}\text{H}_{22} + \text{H} = \text{C}_{10}\text{H}_{21} + \text{H}_2$ (WARNATZ)	3.0E14	0.0	8457.
98.	$\text{C}_{10}\text{H}_{22} + \text{O} = \text{C}_{10}\text{H}_{21} + \text{OH}$ (WARNATZ)	1.0E14	0.0	4539.
99.	$\text{C}_{10}\text{H}_{22} + \text{OH} = \text{C}_{10}\text{H}_{21} + \text{H}_2\text{O}$ (WARNATZ)	1.0E13	0.0	883.
100.	$\text{C}_{10}\text{H}_{22} + \text{CH}_3 = \text{C}_{10}\text{H}_{21} + \text{CH}_4$ (PITZ)	2.0E11	0.0	9500.
101.	$\text{C}_{10}\text{H}_{22} + \text{C}_2\text{H}_3 = \text{C}_{10}\text{H}_{21} + \text{C}_2\text{H}_4$ (PITZ)	3.0E11	0.0	1800.
102.	$\text{C}_{10}\text{H}_{22} + \text{O}_2 = \text{C}_{10}\text{H}_{21} + \text{HO}_2$	2.51E13	0.0	49000.
103.	$\text{C}_{10}\text{H}_{21} - \text{C}_5\text{H}_{11} + \text{C}_5\text{H}_{10}$ (WARNATZ)	2.5E13	0.0	28715
104.	$\text{C}_5\text{H}_{11} - 2\text{C}_2\text{H}_4 + \text{CH}_3$	2.5E13	0.0	28715
105.	$\text{C}_5\text{H}_{10} + \text{H} = \text{C}_2\text{H}_4 + \text{C}_3\text{H}_5 + \text{H}_2$ (WESTBROOK)	5.0E13	0.0	3900.
106.	$\text{C}_5\text{H}_{10} + \text{O} = \text{C}_2\text{H}_4 + \text{C}_3\text{H}_5 + \text{OH}$ (WESTBROOK)	5.0E13	0.0	3900.
107.	$\text{C}_5\text{H}_{10} + \text{OH} = \text{C}_2\text{H}_4 + \text{C}_3\text{H}_5 + \text{H}_2\text{O}$ (WESTBROOK)	5.0E13	0.0	3900.
108.	$\text{C}_5\text{H}_{10} + \text{CH}_3 = \text{C}_2\text{H}_4 + \text{C}_3\text{H}_5 + \text{CH}_4$ (WESTBROOK)	5.0E13	0.0	3900.
109.	$\text{C}_5\text{H}_{10} + \text{C}_2\text{H}_3 = 2\text{C}_2\text{H}_4 + \text{C}_3\text{H}_5$ (WESTBROOK)	5.0E13	0.0	3900.
110.	$\text{C}_3\text{H}_5 = \text{C}_3\text{H}_4 + \text{H}$	3.98E13	0.0	70000.
111.	$\text{C}_3\text{H}_5 + \text{O}_2 = \text{C}_3\text{H}_4 + \text{HO}_2$	6.03E11	0.0	10000.
112.	$\text{C}_3\text{H}_4 + \text{O} = \text{CH}_2\text{O} + \text{C}_2\text{H}_2$	1.0E12	0.0	0.0
113.	$\text{C}_3\text{H}_4 + \text{OH} = \text{CH}_2\text{O} + \text{C}_2\text{H}_3$	1.0E12	0.0	0.0
114.	$\text{C}_3\text{H}_4 + \text{H} = \text{CH}_3 + \text{C}_2\text{H}_2$	2.0E13	0.0	2411
115.	$\text{C}_3\text{H}_4 + \text{O} = \text{CO} + \text{C}_2\text{H}_4$	1.4E13	0.0	2103

116.	C7H8+O2-C6H6+CH2O+O (GUERRET)	1.0E18	0.0	50000.
117.	C8H10+O2-C7H8+CH2O+O (GUERRET)	1.0E18	0.0	50000.
118.	C9H12+O2-C8H10+CH2O+O (GUERRET)	1.0E16	0.0	50000.
119.	C6H6=PHENYL+H (JACKSON AND LAURENDAU)	5.0E15	0.0	108000.
120.	C6H6+H=PHENYL+H2 (JACKSON AND LAURENDAU)	3.0E12	0.0	8100.
121.	C6H6+O=PHENYL+OH	2.8E13	0.0	4910.
122.	C6H6+OH=PHENYL+H2O	2.1E13	0.0	4570.
123.	PHENYL+O2-2CO+C2H2+C2H3	1.1E15	0.0	24000.

APPENDIX B

The variance of χ_{st} , VAR, is given by the expression

$$\text{VAR} = \langle \chi_{st}^2 \rangle - \langle \chi_{st} \rangle^2 \quad (B-1)$$

where $\langle \chi_{st}^2 \rangle$ and $\langle \chi_{st} \rangle$ are the first and second moments of χ_{st} , respectively.

$$\langle \chi_{st}^2 \rangle = \int_0^\infty \chi_{st}^2 P(\chi_{st}) d\chi_{st} \quad (B-2)$$

$$\langle \chi_{st} \rangle = \int_0^\infty \chi_{st} P(\chi_{st}) d\chi_{st}$$

Substituting the expression for the marginal density,

$$\langle \chi_{st}^2 \rangle = \int_0^\infty \chi_{st}^2 \int_0^1 P(\chi_{st}, z) dz d\chi_{st} \quad (B-3)$$

and

$$\langle \chi_{st} \rangle = \int_0^\infty \chi_{st} \int_0^1 P(\chi_{st}, z) dz d\chi_{st}$$

Substituting χ/f for χ_{st} and changing the integration variable yields the following expressions for the first two moments,

$$\langle \chi_{st}^2 \rangle = \langle \chi^2 \rangle \int_0^1 \frac{1}{f^2(z)} P(z) dz \quad (B-4)$$

$$\langle \chi_{st} \rangle = \langle \chi \rangle \int_0^1 \frac{1}{f(z)} P(z) dz$$

$\langle \chi^2 \rangle$ and $\langle \chi \rangle$ are found through the analytical expression for the moments of the lognormal distribution, (Ref.)

$$\langle \chi^2 \rangle = \exp(2\mu + \sigma^2) \cdot (\exp \sigma^2 - 1) \quad (B-5)$$

$$\langle \chi \rangle = \exp(\mu + \frac{1}{2}\sigma^2)$$

Based on experimental data, σ is assumed equal to unity. $\langle \chi \rangle$ is computed in the mean flow calculation; thus, μ is known. The integrals in z space can be evaluated analytically to compute VAR at each point. However, for purposes of estimating the interval of integration for χ_{st} , the following approximations were made,

$$\int_0^1 \frac{1}{f^2(z)} P(z) dz = \langle \frac{1}{f^2(z)} \rangle \simeq \frac{1}{f^2(\bar{z})} \quad (B-6)$$

$$\int_0^1 \frac{1}{f(z)} P(z) dz = \langle \frac{1}{f(z)} \rangle \simeq \frac{1}{f\langle z \rangle}$$

Hence,

$$\text{VAR} = \langle \chi^2 \rangle \frac{1}{f^2 \langle z \rangle} - \langle \chi \rangle^2 \left(\frac{1}{f \langle z \rangle} \right)^2$$

and the standard deviation of χ_{st} , SD, is

$$\text{SD} = \text{VAR}^{1/2} \quad (B - 7)$$

It was found an integration interval from $\chi_{st}=0$ to $\chi_{st}+4\text{SD}$ was sufficient.

REPORT DOCUMENTATION PAGE			Form Approved OMB No. 0704-0188	
Public reporting burden for this collection of information is estimated to average 1 hour per response, including the time for reviewing instructions, searching existing data sources, gathering and maintaining the data needed, and completing and reviewing the collection of information. Send comments regarding this burden estimate or any other aspect of this collection of information, including suggestions for reducing this burden, to Washington Headquarters Services, Directorate for Information Operations and Reports, 1215 Jefferson Davis Highway, Suite 1204, Arlington, VA 22202-4302, and to the Office of Management and Budget, Paperwork Reduction Project (0704-0188), Washington, DC 20503.				
1. AGENCY USE ONLY (Leave blank)	2. REPORT DATE March 1998	3. REPORT TYPE AND DATES COVERED Final Contractor Report		
4. TITLE AND SUBTITLE Turbulent Radiation Effects in HSCT Combustor Rich Zone		5. FUNDING NUMBERS WU-537-05-20-00 NAS3-26618		
6. AUTHOR(S) Robert J. Hall, Alexander Vranos, and Weiduo Yu				
7. PERFORMING ORGANIZATION NAME(S) AND ADDRESS(ES) United Technologies Research Corporation, Pratt & Whitney East Hartford, Connecticut 06108		8. PERFORMING ORGANIZATION REPORT NUMBER E-11021		
9. SPONSORING/MONITORING AGENCY NAME(S) AND ADDRESS(ES) National Aeronautics and Space Administration Lewis Research Center Cleveland, Ohio 44135-3191		10. SPONSORING/MONITORING AGENCY REPORT NUMBER NASA CR-1998-206532		
11. SUPPLEMENTARY NOTES Robert J. Hall, United Technologies Research Corporation, Pratt & Whitney, East Hartford, Connecticut 06108; Alexander Vranos and Weiduo Yu, University of Connecticut, Storrs, Connecticut 06269. Project Manager, Robert R. Tacina, Turbomachinery and Propulsion Division, NASA Lewis Research Center, organization code 5830, (216) 433-3588.				
12a. DISTRIBUTION/AVAILABILITY STATEMENT Unclassified - Unlimited Subject Category: 07 This publication is available from the NASA Center for AeroSpace Information, (301) 621-0390.			12b. DISTRIBUTION CODE	
13. ABSTRACT (Maximum 200 words) A joint UTRC-University of Connecticut theoretical program was based on describing coupled soot formation and radiation in turbulent flows using stretched flamelet theory. This effort was involved with using the model jet fuel kinetics mechanism to predict soot growth in flamelets at elevated pressure, to incorporate an efficient model for turbulent thermal radiation into a discrete transfer radiation code, and to couple the soot growth, flowfield, and radiation algorithms. The soot calculations used a recently developed opposed jet code which couples the dynamical equations of size-class dependent particle growth with complex chemistry. Several of the tasks represent technical firsts; among these are the prediction of soot from a detailed jet fuel kinetics mechanism, the inclusion of pressure effects in the soot particle growth equations, and the inclusion of the efficient turbulent radiation algorithm in a combustor code.				
14. SUBJECT TERMS Combustors; Combustion; Radiation			15. NUMBER OF PAGES 81	
			16. PRICE CODE A05	
17. SECURITY CLASSIFICATION OF REPORT Unclassified	18. SECURITY CLASSIFICATION OF THIS PAGE Unclassified	19. SECURITY CLASSIFICATION OF ABSTRACT Unclassified	20. LIMITATION OF ABSTRACT	